CZECH TECHNICAL UNIVERSITY IN PRAGUE

FACULTY OF BIOMEDICAL ENGINEERING

Department of Biomedical Technology

Určení elektrických vlastností tkání postižených CMP ze snímků z magnetické rezonance - testování na zajednodušených fantomech hlavy

Extraction of Electrical Properties of Strokes from Magnetic Resonance Scans - Testing on Simplified Head Phantoms

MASTER'S THESIS

Study Program:	Biomedical and Clinical Technology
Field of Study:	Biomedical Engineering

Author:	Luis Felipe Díaz Rondón
Supervisor:	doc. Dr.-Ing. Jan Vrba, M.Sc.

Kladno 2017

Department of Biomedical Technology | Academic year: 2016/2017

Diploma thesis assignment

(Master project thesis assignment)

Student:	**Luis Díaz**
Study branch:	Biomedical Engineering (CEMACUBE)
Title:	**Extraction of Electrical Properties of Strokes from Magnetic Resonance Scans – Testing on Simplified Head Phantoms**
Title in Czech:	Určení elektrických vlastností tkání postižených CMP ze snímků z magnetické rezonance – testování na zajednodušených fantomech hlavy

Instructions for processing:

Design and manufacture phantoms mimicking electrical permittivity and conductivityof haemorrhagic and ischemic stroke-affected tissues. Measure electrical properties of manufactured phantoms using commercial measurement system. Design and manufacture head phantom containing phantoms of haemorrhagic and ischemic stroke. Use current methods of magnetic resonance based electrical properties tomography (MREPT) to implement a MATLAB code for extraction of relative permittivity and electrical conductivity from MRI scans. Perform MRI scan of head phantom and extract relative permittivity and electrical conductivity of stroke phantoms using the MATLAB code, and verify results by comparing with previously measured values.

References:

[1] S. K. Lee, S. Bulumulla, P. Lamb, and I. Hancu, Measurement of electrical properties of biological tissue at radio frequencies using magnetic resonance imaging, in 9th European Conference on Antennas and Propagation (EuCAP), ročník 1, číslo 2015, 2015, 1-4 s.
[2] X. Zhang, J. Liu, B. He, Magnetic-Resonance-Based Electrical Properties Tomography: A Review, IEEE Reviews in Biomedical Engineering, ročník 7, číslo 2014, 2014, 87-96 s.

Validity of assignment until date:	20.08.2018
Supervisor of diploma thesis:	doc. Dr. Ing. Jan Vrba, MSc.
Consultant of diploma thesis:	Ing. David Vrba, Ph.D.

..... Head of Department

..... Dean

In Kladno, 20.02.2017

Declaration

I hereby declare that I have developed and written the enclosed Master's Thesis titled: *Extraction of Electrical Properties of Strokes from Magnetic Resonance Scans - Testing on Simplified Head Phantoms* completely by myself, and have not used sources or means without declaration in the text. Any thoughts from others or literal quotations are clearly marked and list of references is enclosed. I have no objection to the usage of this work in compliance with the act x60 of Law No.121/2000 Coll. about copyright and laws related to the copyright and about the changes of certain laws.

In Kladno 18.08.2017 . . . .

Luis Felipe Díaz R.

Acknowledgements

I would like to express great gratitude towards my supervisor, doc. Dr.-Ing. Jan Vrba, M.Sc., not only for his guidance in many areas of this entire process, but also for giving me the opportunity to work on such a challenging topic. I would also like to give many thanks to Ing. David Vrba, Ph.D., for his great collaboration and contribution in the numerical analysis simulations; to doc. Ing. Jaroslav Tintěra, CSc., for taking the time in his busy schedule to assist us during the MRI scans at NUDZ and at IKEM; and finally to my colleagues B.Sc. Yanina Kuzminich and B.Sc. Zuzanna Magnuska, for providing me with tools and information that significantly influenced the satisfactory results reported in this work.

Abstrakt

Několik studií [1, 2] uvádělo značné rozdíly v dielektrických vlastnostech mezi zdravými a patologickými tkáněmi. Kromě toho v oblasti aplikací elektromagnetického pole v medicíně probíhají diskuse o správnosti dielektrických vlastností biologických tkání měřená ex vivo (nejběžnější metoda měření), například kvůli nižšímu prokrvení. Pomocí vlastního principu elektromagnetické činnosti magnetických rezonančních (MR) systémů mohou být změny šíření vln využívány k získání hodnot dielektrických vlastností cílových tkání z MR obrazů a proto také k detekci a klasifikaci nemocí. Tato metoda tedy představuje metodu pro neinvazivní měření dielektrických vlastností biologických tkání in Vivo. V literatuře [3, 4] bylo ukázáno, že jak velikost tak fáze MR RF vln lze stanovit pomocí standardních MR zobrazovacích sekvencí. Použitím výsledné velikosti a fáze RF vln lze dielektrické vlastnosti určit jednoduchým použitím Helmholtzovy rovnice. V této studii tyto zprávy potvrzujeme pomocí numerických simulací s použitím anatomického hlavového modelu s vysokým rozlišením a modelu objemové cívky. Navíc byl navržen a vyroben zjednodušený implantát dielektrických vlastností mozkových tkání a byla zpracována informace z reálných MR snímků. Jak bude ukázáno v této práci, tento proces funguje dobře pro data získaná pomocí numerických simulací, ale není to tak jednoduché pro obrazy pocházející z MR systému. Proto je důležité další zpracování za účelem kompenzace přítomnosti šumu a fázové korekce.

Klíčová slova

Elektrické vlastnosti, MREPT, elektrická vlastnost tomografie, tkáňová klasifikace, neinvazivní, MRI, in vivo.

Abstract

Several studies [1, 2] have reported considerable differences in dielectric properties between healthy and pathological tissues. Various methods for non-invasive electrical properties mapping have been studied and applied with acceptable results but with complex and clinically unrealistic setups. By using the inherent electromagnetic working principle of magnetic resonance (MR) systems, changes in wave propagation can be used to extract values of dielectric properties of target tissues from MR images, and therefore, detect and classify abnormalities. This method thus represents a method for non-invasive measurement of dielectric properties of biological tissues in Vivo. It has been show in literature [3, 4] that both magnitude and phase of the MR RF waves can be determined using standard MR imaging sequences. By using the resulting magnitude and phase of RF waves dielectric properties can be determined by simply using the Helmholtz equation. In this study we confirm such reports through numerical simulations using high-resolution anatomical head model and a model of bird-cage coil. Furthermore, a simplified head phantom mimicking dielectric properties of strokes and brain tissues was designed and manufactured and information from real MR scans was processed. As it will be shown in this work, this process works well for data obtained via numerical simulations but it is not as straightforward, for the images coming from the MR system. There, additional processing in order to compensate for the presence of noise and de-phasing is crucial.

Keywords

Electrical properties, MREPT, electrical property tomography, tissue classification, non-invasive, MRI, in vivo.

Contents

List of acronyms

Acronym	Meaning
CT	Computed Tomography
DW-MRI	Diffusion-weighted Magnetic Resonance Imaging
EM	Electro Magnetic
EP	Electrical Property
EIT	Electrical Impedance Tomography
EPT	Electrical Property Tomography
FLAIR	Fluid-attenuated Inversion Recovery
HTP	Hyperthermia Treatment Planning
MAT-MI	Magneto-acoustic Tomography with Magnetic Induction
MR	Magnetic Resonance
MIT	Magnetic Induction Tomography
MRA	Magnetic Resonance Angiography
MRI	Magnetic Resonance Imaging
MREIT	Magnetic Resonance Electrical Impedance Tomography
MREPT	Magnetic Resonance based Electrical PropertyTomography
PW-MRI	Perfusion-weighted Magnetic Resonance Imaging
RF	Radio Frequency
ROI	Region of interes
SAR	Specific Absorption Ratio
SNR	Signal-to-Noise ratio

List of symbols

Symbol	Units	Meaning
B	T	Magnetic flux density
E	$\mathrm{V} \cdot \mathrm{m}$	Electric field intensity
D	$\mathrm{C} \cdot \mathrm{m}^{-2}$	Electric flux density
J	$\mathrm{A} \cdot \mathrm{m}^{-2}$	Current density
H	$\mathrm{A} \cdot \mathrm{m}^{-1}$	Magnetic field intensity
ε	$\mathrm{F} \cdot \mathrm{m}^{-1}$	Permittivity
ε_r	–	Relative Permittivity
ε_0	$\mathrm{F} \cdot \mathrm{m}^{-1}$	Permittivity of free-space
μ	$\mathrm{H} \cdot \mathrm{m}^{-1}$	Magnetic permeability
μ_0	$\mathrm{H} \cdot \mathrm{m}^{-1}$	Magnetic permeability of free-space
σ	$\mathrm{S} \cdot \mathrm{m}^{-1}$	Electrical conductivity
ω	$\mathrm{rads} \cdot \mathrm{m}^{-1}$	Angular frequency / Larmor frequency
$f(x)$	–	Function
$\partial^2/\partial x$	–	Second partial derivative
∇^2	–	Laplacian operator
γ	–	Complex propagation constant
ϵ_1	–	First-order phase error term
ϕ_0	–	Second-order phase error term
E	–	Statistical expectation
Z	–	Statistical normal distribution factor
σ^2	–	Statistical variance
ρ_x	–	Autocorrelation of adjacent pixels in $x-$direction
I	–	GRE low-flip-angle image intensity
I_0	–	Real GRE low-flip-angle image intensity
I_{GRE}	–	GRE low-flip-angle image intensity
$\measuredangle I_{SE}$	rads	Phase of SE image intensity
B_1^+	T	Transmit component of transverse RF field in MRI
B_1^-	T	Receive component of transverse RF field in MRI
$\measuredangle B_1^+$	rads	Phase of transmit component of transverse RF field in MRI
$\measuredangle B_1^-$	rads	Phase of receive component of transverse RF field in MRI

1 Introduction

Assuming that different type of tissues have different electrical properties (EPs), then tissue characterization is possible based on electromagnetic (EM) wave propagation. By using the inherent EM working principle in magnetic resonance imaging (MRI), an applied and further detected EM wave is used for tissue electrical properties mapping in-vivo.

1.1 Electrical Properties of Tissues

Biological tissues contain and work with charged particles. When these are exposed to electromagnetic fields, currents are induced and wave propagation experiences modifications within the medium in comparison to that of free space [5].

There are three basic constitutive parameters which are used to classify a material by its electrical properties:

1. Relative Permittivity (ε_r)
2. Electrical Conductivity (σ)
3. Magnetic Permeability (μ)

These constitutive parameters (EPs) are in general valued depending on direction and strength of the applied field, frequency, and position within the material or medium [5]. When a material's electrical properties are not a function of position, such are referred to as being homogeneous, otherwise they are in-homogenous or non-homogenous [5], which as it will be seen further, will be a characteristic of most importance for the procedures performed and described in this document.

1.1.1 Relative Permittivity (ε_r)

When an external electric field $\overrightarrow{E}$ is applied to a material, this exerts a force on its internal electric dipoles forcing them to align with the external field. This alignment generates an internal electric field that opposes the external one reducing its overall magnitude. Permittivity of a material can be understood as how easily the dipoles of a material rotate to align with an externally applied electric field and therefore oppose to it. The difference between electric field lines that enter and exit a material will depend on the value of permittivity of that specific material [6]. Permittivity ε is the constant of proportionality that determines the exiting electric field lines (electric flux density $\overrightarrow{D}$) when an externally

applied electric field $\overrightarrow{E}$ exists over a material (Eq. 1). Parameter ε is called the absolute permittivity of a medium, or material [7],

$$\overrightarrow{D} = \varepsilon \overrightarrow{E}. \tag{1}$$

Permittivity also shows a material's capacity to store charge [6], the larger the permittivity, the larger its capacity to store charge [5].

Relative permittivity (also called Dielectric Constant) is a dimensionless value given when the medium's absolute permittivity is compared to that of free space [5],

$$\varepsilon_r = \frac{\varepsilon}{\varepsilon_0}. \tag{2}$$

For free space, permittivity has the approximate value of $\varepsilon_0 = 8.854 \times 10^{-12}$ F $\cdot$ m^{-1} [7].

1.1.2 Electrical Conductivity (σ)

Conductivity is a property that measures the ability of a charged particle to travel along a material (medium or tissue), when influenced by, and in the direction of, an externally applied electric field [6]. The amount of electric charge, flowing per unit area is known as the current density $\overrightarrow{J}$, and its proportionality with the electric field $\overrightarrow{E}$ is weighted by the factor σ [7],

$$\overrightarrow{J} = \sigma \overrightarrow{E}. \tag{3}$$

1.1.3 Magnetic Permeability (μ)

The third one of the mentioned basic constitutive parameters of materials. It serves as an indicator of the ability of a medium to be magnetized by an externally applied magnetic field. The number of magnetic field lines across a given surface $\overrightarrow{B}$(magnetic flux density) due to a magnetic field $\overrightarrow{H}$, is weighted down by the factor μ [7],

$$\overrightarrow{B} = \mu \overrightarrow{H}. \tag{4}$$

Permeability values for biological tissues are generally assumed to approximate that of free space ($\mu \approx \mu_0$) [8, 9]. For free space, permeability has a value of $\mu_0 = 4\pi \times 10^{-7}$ H $\cdot$ m^{-1} [7].

From now on, whenever it is referred to electrical properties (EPs) in this document, the parameters considered will be only relative permittivity (ε_r) and electrical conductivity (σ).

1.2 Importance of Measuring EPs

EPs of biological tissues characterize charged particles movement and EM wave propagation through the body, therefore, are very important for a wide range of diagnostic and therapeutical applications used today which are based on weak electrical currents and electromagnetic fields. EPs are needed in order to accurately forecast biological responses to electromagnetic stimulations. [6]

Local radio frequency (RF) power deposition, better know as the Specific Absorption Rate (SAR), has been a critical topic regarding all that is concerned with human biology exposed to electromagnetic radiation. SAR is proportional to the electrical conductivity σ of the medium and the square of the applied electric field. For widely used biomedical applications like MRI, SAR is of significant importance because it assists in evaluating potential hot spots during scanning, especially with higher fields being used (7T) and with the use of multiple transmitters. For therapeutical applications like RF Hyperthermia, numerical simulations are done during the Hyperthermia Treatment Planning (HTP) in order to quantify the SAR on a spatially focused electromagnetically-heated area. This is done in order to establish parameters to increase energy on target tissue, while avoiding as much damage possible to surrounding healthy tissue [9]. Currently, a fixed value of electrical conductivity is used for all tumor types (muscle conductivity of 0.72 $\mathrm{S} \cdot \mathrm{m}^{-1}$ at 128MHz), when it has been already reported that tumors' elevated conductivity values vary greatly among patients [10]. This variation affects accuracy of predicted SAR values and therefore limits the accuracy of the treatment [11].

Tissue EPs may also serve as indicators for diagnosing malignancies as there are reported differences in EP values between healthy and unhealthy tissues [9]. Typical differences in relative permittivity and electrical conductivity values, of normal to malignant tissue, vary from 10% to 20% for variety of tissue types. However, for breast cancerous tissue, it has been reported an increase in permittivity of three times its normal value [12]. Other studies show EPs differences from healthy to unhealthy tissues around 5% over the frequency range for tissues like the kidney, and around 233% and 577% for permittivity and conductivity respectively for the mammary gland [1]. In another study, In-vivo conductivity values of glioma are compared to measured conductivity values of white matter of healthy volunteers. Glioma's conductivity was found to be significantly higher than that of healthy white matter [13].

The contrast in EPs from normal to malignant tissue, is significantly greater than that given by other imaging modalities like X-ray or Ultrasound, therefore suggesting a better approach for the objective of both detecting and characterizing cancerous tissue. [14]

Ex-vivo studies also suggest value in diagnostic of strokes, as it has been reported in [15] to exist significant changes in both permittivity and conductivity of affected brain tissue.

In clinical practice, a method that could be able to accurately map EPs in-vivo, non-invasively and with very low energy deposition, would be very useful for a wide range of biomedical applications.

1.3 State of the art in EPs extraction methods

Due to biological tissue complexity, measuring EPs of biological tissues in-vivo have become a great challenge for the interested research community. Most of the methods designed and researched have great complexities in terms of used equipment and computation [6]. Here's a short list of some relevant approaches done far:

Electrical Impedance Tomography (EIT): low frequency currents are applied on the body through a series of electrodes and an inverse problem is solved in order to compute the EPs.

Magnetic Induction Tomography (MIT): similar to EIT but instead of using electrodes uses a coil to induce currents and to receive signals.

MR Electrical Impedance Tomography (MREIT): an improved EIT approach that takes advantage of spatial encoding of MRI for increased resolution.

Magneto-acoustic Tomography with Magnetic Induction (MAT-MI): acoustic waves are collected with ultrasound transducer near the area of interest. This are produced by the Lorentz force effect by an applied time-varying magnetic field.

Microwave Imaging: microwaves are widely used for detection and classification of inner structures taking advantage of the high material penetration and low energy deposition that they offer. However reports have shown that most EP contrast, between normal and abnormal tissues, is found in the frequency range of $\sim$1 KHz to $\sim 10^2$ MHz [16].

A more detailed explanation on these methods for EPs extraction and mapping in-vivo can be found in [16, 17].

Recently, a new method for electrical properties tomography (EPT) has been intro-

duced [3]. This method uses information from B_1^+ field maps generated from the applied RF pulse in MRI, to compute EPs in-vivo at the Larmor frequency [16]. This method is called **Magnetic Resonance based Electrical Properties Tomography(MREPT)**, and will the center approach for EP mapping in this work.

1.4 Advantages of the MREPT method

Changes in EPs for biological tissues can be due to many different reasons. EPs depend on many tissue factors, like concentrations of ions, water, fat and protein. These factors can be greatly altered under abnormal or pathological conditions. Variations in EPs for various types of tissues have been reported at the Larmor frequency of water proton, suggesting that MREPT holds great potential for non-invasive tissue characterization in oncology. [18]

Among the list mentioned, MREIT is one of the most prominent in terms of accuracy, however electrodes mounted while inside the MRI scanner makes it complex and unrealistic for clinical practice. MREPT on the other hand requires no electrode mounting, and no additional energy is deposited into the subject other than that inherent to the MRI procedure. MREPT uses standard RF coils, and resolution of the resulting image will increase or decrease depending on B_1^+ mapping methods. [17]

1.5 Application of MREPT for Stroke detection and classification

Stroke is a term used to characterize a focal disturbance in cerebral function due to a blood supply deficit. For it to be considered a stroke, the neurological dysfunction must last more than 24 hours, unless interrupted by clinical treatment or death, and should be of vascular cause and not by injury [19, 20]. There are two basic types of stroke: ischemic and hemorrhagic [21].

An **ischemic** stroke is when brain cells die due to a critically low blood perfusion caused by an occlusion of the supply lines: arteries, small arteries, or venous sinuses. Usually this critical reduction in blood supply is due to athero-thrombotic changes of the arteries or by emboli that originate in the heart, the aorta or other large arteries. [20]

A stroke is considered **hemorrhagic** when there's a considerable amount of blood filtered out of the arteries and into the brain parenchyma, or ventricular system, due to ruptures of small arteries, arterial aneurysms, or capillaries. [19]

Strokes need to be primarily classified in order to apply proper treatment. Treating hemorrhagic stroke as, or while being treated for ischemic, will result disastrous as one

stroke treatment promotes worsening of the other. Anti-platelets, and the likes, for example, used for ischemic stroke treatment should not be applied for hemorrhagic situations for they will only promote increasing bleeding [20].

For detection and classification, MRI and computed tomography(CT) are the preferred approaches. Both give accurate information with high resolution images. MRI in particular uses a multi-parametric approach in which different imaging sequences are employed in order to image, localize, classify and understand the origin of an acute-stroke-affected area. Example of sequences used are diffusion-weighted MRI (DW-MRI), perfusion-weighted MRI (PW-MRI), MR angiography(MRA) and fluid-attenuated inversion recovery (FLAIR). [20]

Studies have shown marked changes in electrical properties both for ischemia and infarction [22, 23, 24], making MREPT applicable for stroke detection and classification. Mapping of EPs can also provide hints on the nature, gravity and/or development of the affected areas, before and after treatment as the EPs have shown to change according to state of the affected tissue [24].

1.6 Aim of project

With this project it is intended to prove the validity of the theoretical background in which MREPT is based by performing numerical simulations and MRI scans to accurately map and extract values of EPs from a simplified head phantom representing strokes and brain tissues.

With this effort, it is of the author best interest for this work to become base ground in which future investigations from this faculty, and the university, can work on regarding this topic, or any other EM application in medicine that relates to it.

2 Theory

During magnetic resonance imaging, aligned nuclear spins with the main magnetic field B_0 are taken to another energy level due to spins entering in resonance with an applied RF pulse that oscillates at the Larmor frequency. A signal is perceived on the coil as the RF pulse is turned off and nuclear spins relax back into alignment with B_0. The RF pulse is denoted as the B_1 field, a complex quantity with magnitude and phase, which is composed of two circularly and opposing magnetic field components: B_1^+(transmit) and B_1^-(receive). It is important to note that only B_1^+ is able to induce a flip angle on nuclear spins. In MREPT, information from the MRI signal is used to map B_1^+ field distribution on the scanned sample. From this map, magnitude and phase of B_1^+ are used to compute from the Helmholtz equation the relative permittivity ε_r and the electrical conductivity σ of the biological tissues in-vivo. [17]

2.1 The Helmholtz equation (wave equation)

For MREPT to be successful, the method needs to be applied in a source free, linear, isotropic and homogenous dielectric medium, therefore that use of the wave equation. Considering a charge-free region with homogenous EPs, Maxwell equations in phasor form are

$$\nabla \cdot E = 0 \tag{5}$$
$$\nabla \cdot B = 0 \tag{6}$$
$$\nabla \times E = -\mathrm{j}\omega B \tag{7}$$
$$\nabla \times B = \mu(\sigma + \mathrm{j}\omega\varepsilon)E. \tag{8}$$

By using the vectorial identity

$$\nabla \times \nabla \times A = \nabla(\nabla \cdot A) - \nabla^2 A, \tag{9}$$

and doing the curl on both sides of (8), it is obtained

$$\nabla \times \nabla \times B = \mu(\sigma + \mathrm{j}\omega\varepsilon)\nabla \times E \tag{10}$$
$$\nabla(\nabla \cdot B) - \nabla^2 B = \mu(\sigma + \mathrm{j}\omega\varepsilon)\nabla \times E. \tag{11}$$

Replacing (6) and (7) on (11)

$$-\nabla^2 B = \mu(\sigma + \mathrm{j}\omega\varepsilon)(-\mathrm{j}\omega B) \tag{12}$$
$$-\nabla^2 B = -\mathrm{j}\omega\mu(\sigma + \mathrm{j}\omega\varepsilon)B. \tag{13}$$

Arranging equation (2) gives

$$\nabla^2 B - \gamma^2 B = 0, \tag{14}$$

with

$$\gamma^2 = j\omega\mu(\sigma + \mathrm{j}\omega\varepsilon). \tag{15}$$

Finally, (14) is the wave equation or Helmholtz equation. The Helmholtz equation derivation is very well explained in most literature concerning electro-magnetics theory, the derivation shown above was based on [25]. Concerning scientific notation, the ones used are meant to copy those used in research papers regarding MREPT, as can be seen, for example, in [9].

2.2 Derivation of EPs from the Helmholtz equation

The electrical properties, relative permittivity(ϵ_r) and electrical conductivity(σ), can both be derived from the Helmholtz equation (14). Rearranging

$$\sigma + \mathrm{j}\omega\varepsilon \rightarrow \mathrm{j}\omega\varepsilon\left(1 - \mathrm{j}\frac{\sigma}{\omega\varepsilon}\right). \tag{16}$$

Introducing (16) in (13)

$$-\nabla^2 B = -\mathrm{j}\omega\mu\left(j\omega\varepsilon\left(1 - \mathrm{j}\frac{\sigma}{\omega\varepsilon}\right)\right) B \tag{17}$$

$$-\nabla^2 B = \omega^2\mu\varepsilon\left(1 - \mathrm{j}\frac{\sigma}{\omega\varepsilon}\right) B \tag{18}$$

$$-\frac{\nabla^2 B}{B} = \omega^2\mu\varepsilon - \mathrm{j}\omega\mu\sigma. \tag{19}$$

Taking the real part of equation (19)

$$-Re\left\{\frac{\nabla^2 B}{B}\right\} = \omega^2\mu\varepsilon, \tag{20}$$

$\epsilon = \epsilon_r\epsilon_0$, and $\mu = \mu_0$ (assumed for biological tissue), then 1.16 becomes

$$\varepsilon_r = -\frac{1}{\omega^2\mu_0\varepsilon_0} Re\left\{\frac{\nabla^2 B}{B}\right\}. \tag{21}$$

Next, the imaginary part of equation (19) is taken:

$$-Im\left\{\frac{\nabla^2 B}{B}\right\} = -\omega\mu\sigma. \tag{22}$$

Also assuming $\mu = \mu_0$, equation (22) is solved for

$$\sigma = \frac{1}{\omega\mu_0} Im\left\{\frac{\nabla^2 B}{B}\right\}. \tag{23}$$

As said before, in nuclear magnetic resonance only the B_1^+ component of the RF wave resonates with the protons precessing at the Larmor frequency, therefore

$$\varepsilon_r = -\frac{1}{\omega^2\mu_0\varepsilon_0} Re\left\{\frac{\nabla^2 B_1^+}{B_1^+}\right\}, \tag{24}$$

$$\sigma = \frac{1}{\omega\mu_0} Im\left\{\frac{\nabla^2 B_1^+}{B_1^+}\right\}. \tag{25}$$

Equations (24) and (25) are the basic equations for tissue electrical properties extraction in Magnetic Resonance Imaging (MREPT equations), where ω is the Larmor frequency in $\text{rads} \cdot \text{s}^{-1}$, and ϵ_0 $(-)$ and μ_0 $(\text{H} \cdot \text{m}^{-1})$ are the permittivity and permeability in vacuum respectively.

2.3 B_1^+ mapping with MRI

B_1^+ fields are the basic step forward into electrical properties mapping. Over the years, there has been great focus on research to correctly create B_1^+ field maps from MRI scans. Many methods have been established in which the magnitude has been mathematically derived from received signals in MRI. However, for the phase component of B_1^+, there's has been no success in accurately deriving it from the same source. B_1^+ phase acquisition has been a considerable problem in MREPT because there's no standard method that could supply it, instead, approximations based on certain conditions have been used in order to infer its absolute value [17]. Current B_1^+ field mapping methods fail to provide a reliable B_1^+ phase value, they have low resolution and lower SNR compared to that of standard MRI images [26].

Approximated values for B_1^+ magnitude and B_1^+ phase can be extracted separately from standard MRI sequences [26], therefore providing B_1^+ data information with higher SNR and also making it more realistic for clinical practice.

2.4 B_1^+ magnitude and phase from standard MR images

As shown and demonstrated on [26, 27, 28], equations (24) and (25) can be approximated as follows,

$$\varepsilon_r \approx -\frac{1}{\omega^2 \mu_0 \varepsilon_0} Re\left\{ \frac{\nabla^2 \sqrt{B_1^+ B_1^-}}{\sqrt{B_1^+ B_1^-}} \right\}, \tag{26}$$

$$\sigma \approx \frac{1}{\omega \mu_0} Im\left\{ \frac{\nabla^2 \sqrt{B_1^+ B_1^-}}{\sqrt{B_1^+ B_1^-}} \right\}. \tag{27}$$

This approximation is advantageous because both magnitude and phase of the product $B_1^+ B_1^-$ can be easily derived from MR standard images, avoiding then the complex process of B_1^+ mapping [27]. The complex image intensity from a low-flip-angle Gradient Recall Echo (GRE) sequence in MRI is given by the following expression:

$$I = I_0 B_1^+ B_1^-. \tag{28}$$

I is the complex image intensity, I_0 the real image intensity that results from proton density and other tissue contrasts, and $B_1^+ B_1^-$ is a weighting factor that affects the resulting image intensity, contamination influenced by the applied transverse magnetic field. There is a lot of research being done in order to remove the $B_1^+ B_1^-$ component out of the equation, as it promotes image shading. However, for MREPT, proves to be beneficial. By inserting (28) in (26) and (27), a method is obtained in which derivation of EPs in-vivo is possible solely from standard MR images. It is appropriate to remind the reader that the mentioned formulas for EP estimation can only apply where values of electrical properties are expected to be constant in every point of the target zone. With this in mind, I_0 can be assumed to vary so slowly as to be considered a constant so it factors out of the Laplacian operator and cancels out in the fraction. [27]

The utilization of low-flip-angle spoiled GRE, provides a complex image in which we can square root the magnitude component to obtain B_1^+ magnitude. However, for B_1^+ phase, image can be negatively influenced by spatially varying phase values due to B_0 inhomogeneities. Therefore, for B_1^+ phase a separate imaging sequence needs to be applied. [27]

Spin echo (SE) imaging is beneficial for phase mapping as it is unaffected by the above mentioned issue. By using then a separate spin echo (SE) sequence, a phase image that could be used for estimation of B_1^+ phase can be obtained [26, 27, 28, 9]. The absolute phase value of an MR signal can be seen as the sum of the phases of transmit(B_1^+) and receive(B_1^-) signals, commonly known as the transceive phase [17]. Under the assumption

that both B_1^+ and B_1^- have the same phase, then

$$\measuredangle B_1^+ \approx \frac{1}{2}(\measuredangle B_1^+ + \measuredangle B_1^-), \tag{29}$$

where $\measuredangle B_1^+ + \measuredangle B_1^-$ corresponds the phase image of a SE sequence in a switched mode, quadrature birdcage coil. Under sample's certain symmetry conditions, the relationship in (29) was shown to be exact. [27, 9]

To establish a complex number the accurately represents the product $B_1^+ B_1^-$ two separate MRI sequence would be needed: GRE low-flip-angle and SE. Conceptually, the square root in equations (26) and (27) can then be equivalent to the following

$$\sqrt{B_1^+ B_1^-} \rightarrow \sqrt{|I_{GRE}|} \cdot exp(\frac{1}{2}\measuredangle I_{SE}), \tag{30}$$

where I_{GRE} andI_{SE} are the image intensity values of magnitude of GRE and phase of SE respectively.

The mathematical background that explains the above mentioned formulas and assumptions is out of the scope of this thesis. If the reader is interested, information can be found in references [3, 4, 29].

3 Methods

3.1 Phantom design and manufacturing

First step on this project: construction of our individual phantoms mimicking EPs of strokes and brain tissues. Strokes don't posses standard EP values, for they are complex states in which biological tissues can transform and its qualities depend on many factors like: the type of lesion, affected area, and time from onset of the lesion. Some studies have performed EP measurements for these type of affections ex-vivo. This will the basis for the values selected for this project [23].

For ischemic stroke, study [2] suggests values for relative permittivity and conductivity for wide range of frequency values. In this, there's a decrease in 20% for conductivity and a decrease of 10% for relative permittivity of the affected tissue compared to its own in normal state. White matter will be used as reference for normal healthy tissue, and by reducing its relative permittivity by 10% it yields a new value that can be used as an ischemic stroke phantom. For its conductivity value, the 20% decrease won't be used, instead, 50% decrease of white matter conductivity will be selected arbitrarily in order to reduce the value so the MREPT method can be checked on really small values as well.

For hemorrhagic stroke, its permittivity and conductivity values are generally assumed to be that of blood on normal state [30, 31, 32, 33]. Electrical properties of blood at frequency 123 MHz, are taken directly from IT'IS foundation data base [34]. Table 1 shows selected EP values for the experiments that took place.

Table 1: *Defined values for samples' relative permittivity and electrical conductivity.*

Samples	ε_r $(-)$	σ $\left(\mathrm{S}\cdot\mathrm{m}^{-1}\right)$
Ischemic Stroke	47,9	0,17
Hemorrhagic Stroke	73,7	1,25
White matter	53,2	0,34

A third sample representing white matter will be manufactured. This particular tissue is selected because is the major occupying type of tissue in the brain and has the highest probability for stroke occurring. By joining the three individual phantoms, two stroke phantoms and a normal brain tissue phantom, a simplified head phantom is then formed. Applying MREPT to this formation will provide lights on the existence of contrast between them by EP mapping, and so, assure if both detection and classification are possible.

Phantoms were created by mixing distilled water with normal kitchen salt and isopropanol 99,9% vol. Measurement of EPs will done simultaneously with the mixing. Electrical property measurements will be done using a dielectric probe DAK 12 connected to

a KEYSIGHT FieldFox RF Network Analyzer (N9923A). Experimental setup is shown on Fig 1.

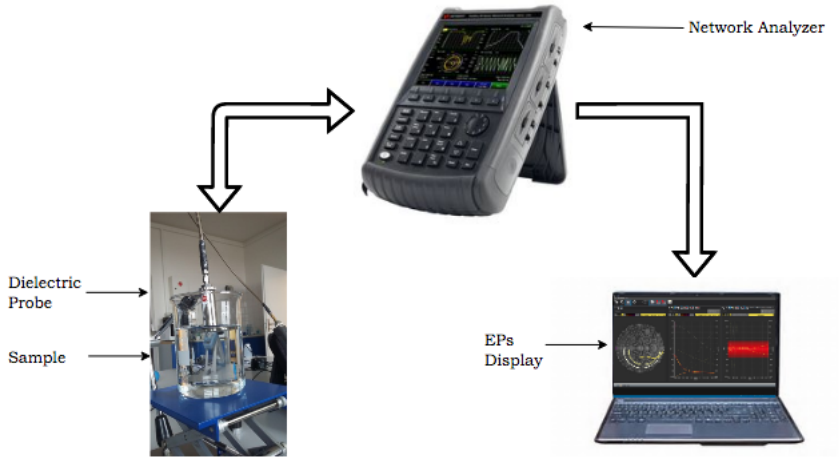

Figure 1: *Experimental setup for EP measurement of samples for head phantom. Network analyzer connects to the sample via the dielectric probe, it sends and receives EM waves at different frequencies. Processed information is then sent to the laptop for proper data visualization.*

3.2 Simulations

Individual samples arranged inside coil

As a first step in our testing of the proposed theory regarding EPT, an exercise will be done involving computational numerical simulations and analysis. Three cylinders with set EPs equal to our previously manufactured samples, will be placed in the space within a coil resembling specifications of that of an MRI RF coil. The goal is to obtain from the simulations proper images of B_1^+ field distribution in space. The obtained data will be processed and equations (24) and (25) will be used to map EPs of the entire field of view. A flow diagram of the entire process can be seen on Fig 2.

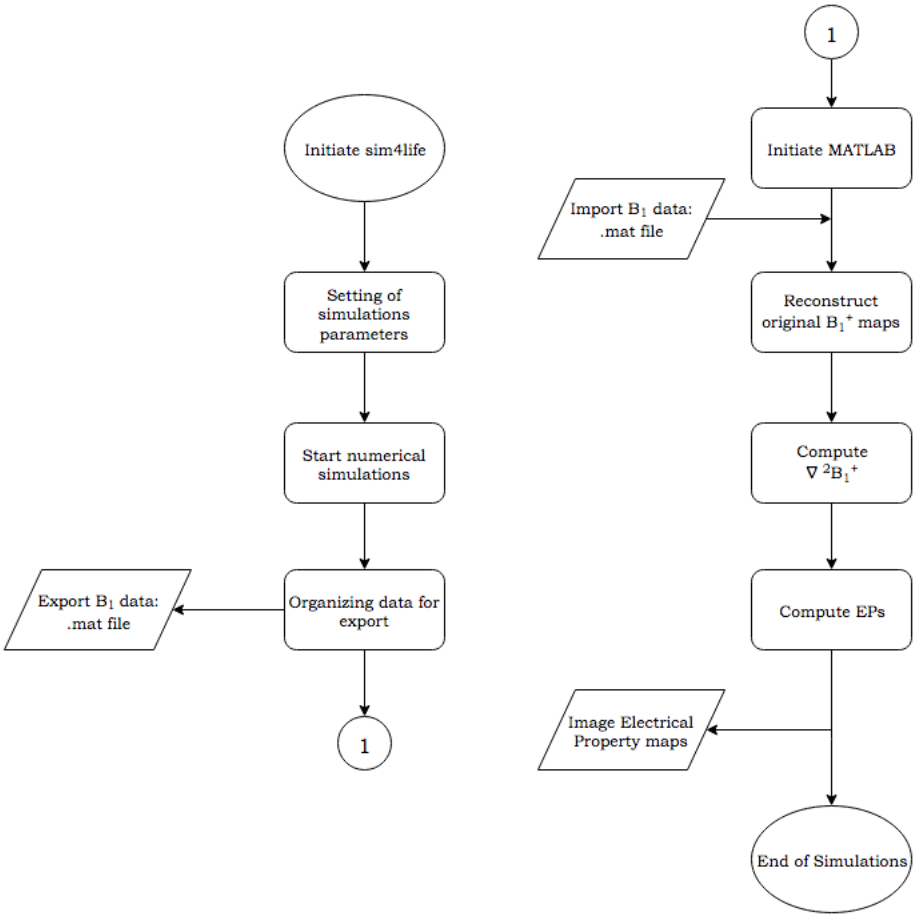

Figure 2: *Simulations' process flow diagram*

The software used for the numerical simulations was sim4life (ZMT, Switzerland). Designed coil was16-rung, shielded low-pass birdcage coil, with diameter 28cm, rung length 28cm and rung to shield spacing of 3.5cm. Each rung with unit amplitude current source at the center. The phases of the current sources were assigned a step increment from rung to rung, equal to $2\pi/16$. Overall frequency of the system 128MHz to simulate a 3 Tesla MRI. Coil spec were based on [9].

Once simulations are done, resulting data is exported and then uploaded in MATLAB (MathWorks, USA). Data coming from sim4life (ZMT, Switzerland) is a 4-matrix set: 1 matrix with 2 data columns (col1: B_1^+, col2: B_1^-), and 3 data vectors representing axis information for each direction. Information needs to be properly transformed from the data column of interest, and correctly distributed in the space that is formed by the three axises. Next step is to compute the Laplacian of the transmit magnetic field ($\nabla^2 B_1^+$).

In a data matrix, computation of the Laplacian is relatively simple by using discrete central difference equations. With these, first and/or second derivatives of a set of data in a desired direction can be easily estimated. Equation (31) is typical example of a

derivative calculation using discrete central difference.

$$\frac{\partial^2 B_1^+(i,j,k)}{\partial x^2} = \frac{B_1^+(i,j-2,k) - 2B_1^+(i,j,k) + B_1^+(i,j+2,k)}{4\triangle_x^2} \tag{31}$$

In the equation above, second derivative of the B_1^+ field in the x-direction is estimated using the second-nearest neighbor. Please note that (i,j,k) are used as (rows, columns, slices) of the imaged volume. This equation can be easily set to compute every point in space, and if also y-direction and z-direction are computed, then:

$$\nabla^2 B_1^+(i,j,k) = \frac{\partial^2 B_1^+(i,j,k)}{\partial x^2} + \frac{\partial^2 B_1^+(i,j,k)}{\partial y^2} + \frac{\partial^2 B_1^+(i,j,k)}{\partial z^2}. \tag{32}$$

Through this method, it would be relatively simple to generate an algorithm that would rapidly compute the Laplacian of B_1^+ for every point in space. However, this method relies on every data point to be located at the same distance from each other, meaning same pixel-to-pixel spacing for all the field of view. Numerical computation's software, sim4life (ZMT, Switzerland), did not deliver information in this format. The exported file has data points at different distance from each other, this is the information contained in the axis vectors. Creating an algorithm, for an entire field of view computation of the Laplacian B_1^+, using discrete central difference equations, that will take into account the spacing between pixels at every single location, is the next challenge.

To obtain an equation that satisfies our immediate need, Taylor's Theorem will be used.

$$f(x_0) = p(x_0) + error(\xi) \tag{33}$$

In (33) $p(x_0)$ is a polynomial which approximates to the function f at point x_0, and $e(\xi)$ is the inherent error in the calculation evaluated at point ξ,which is between x and x_0. By expanding the right side of the equation above using the Taylor's series, a formula can be derived for the second derivative of f:

$$f(x_{0+1}) \;=\; f(x_0) + af^{'}(x_0) + \frac{a^2}{2!}f^{''}(x_0) + \frac{a^3}{3!}f^{(3)}(\xi), \tag{34}$$

$$f(x_{0-1}) \quad = \quad f(x_0) - bf^{'}(x_0) + \frac{b^2}{2!}f^{''}(x_0) - \frac{b^3}{3!}f^{(3)}(\xi), \tag{35}$$

where a is the distance to the nearest neighbor data point in the positive direction, and b is the distance to the nearest neighbor data point in the negative (opposite) direction. By doing

$$b \cdot f(x_{0+1}) + a \cdot f(x_{0-1}) \tag{36}$$

second derivative of f at selected point of interest x_0 is derived, and it results as follows:

$$f^{''}(x_0) = \frac{2}{ab(a+b)} \cdot [bf(x_{0+1}) + af(x_{0-1})] - \frac{2}{ab}f(x0) - \frac{(a-b)}{4}f^{(3)}(\xi), \tag{37}$$

where the third term on the right side of the equation represents the error term, which, as can be clearly seen, will grow as the difference between distances of neighboring data points grow. Finally, for proper Laplacian calculation, the following set formulas are used for second partial derivatives of B_1^+:

$$\frac{\partial^2 B_1^+(i,j,k)}{\partial x^2} = \frac{2}{ab(a+b)}[bB_1^+(i,j+1,k) + aB_1^+(i,j-1,k)] - \frac{2}{ab}B_1^+(i,j,k) \tag{38}$$

$$\frac{\partial^2 B_1^+(i,j,k)}{\partial y^2} = \frac{2}{ab(a+b)}[bB_1^+(i+1,j,k) + aB_1^+(i-1,j,k)] - \frac{2}{ab}B_1^+(i,j,k) \tag{39}$$

$$\frac{\partial^2 B_1^+(i,j,k)}{\partial z^2} = \frac{2}{ab(a+b)}[bB_1^+(i,j,k+1) + aB_1^+(i,j,k-1)] - \frac{2}{ab}B_1^+(i,j,k). \tag{40}$$

With these new set of formulas, a proper algorithm for entire field of view of Laplacian of B_1^+ computation can be established for our particular case. $\nabla^2 B_1^+$ is then calculated with (32)

To compute the Laplacian using the second nearest neighbors the equations are similar to the set shown above, only a and b should be replaced with the correspondent distance values of these new data points.

$\nabla^2 B_1^+$ and B_1^+ are substitute on equations (24) and (25) and EP maps are done.

Head model

A real head model is used for EM simulations. This model (Fig. 3) contains well defined layers and EP values at 128MHz are assigned on the model based on [34] (Table 2). Same algorithm explained above applies for EP estimation of head model.

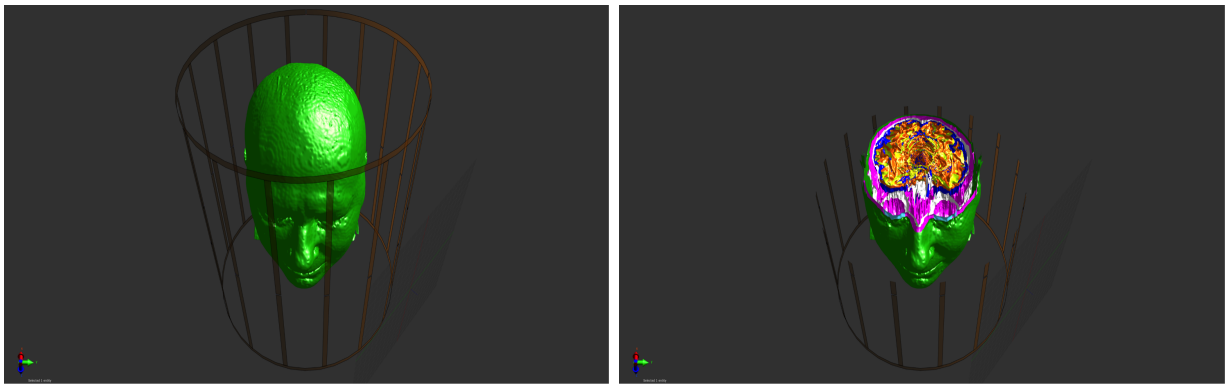

(a) (b)

Figure 3: *Real head model. a) Head model placed inside birdcage coil. b) Head model showing cross-section*

Table 2: *Pre-set electrical property values of tissues contained in the real Head model.*

Assigned Material	Database	ε_r $(-)$	σ $(\mathrm{S \cdot m^{-1}})$
Cerebrospinal Fluid (CSF)	IT'IS 3.1	84,04	2,143
Brain (White matter)	IT'IS 3.1	52,53	0,342
Eye (Vitreous Humor)	IT'IS 3.1	69,06	1,505
Subcutaneous Fat (SAT)	IT'IS 3.1	12,37	0,069
Bone (Cortical)	IT'IS 3.1	14,72	0,067
Skin	IT'IS 3.1	65,44	0,523
Brain (Gray matter)	IT'IS 3.1	73,52	0,587

3.3 MREPT

For real samples and use of MRI scanner in EPT the process is more complex. A flow diagram can be see on Fig. 4.

Phantom Scan on MRI machine

Each liquid sample was enclosed in a plastic recipients of 250ml capacity and secured with a tight lid. The three samples were joined together inside a plastic bag for simple mimicking of normal and affected brain tissues: simplified head phantom. The head phantom was set inside a 3T SIEMENS MRI scanning machine. Two separate scans were

done in order to extract approximate B_1^+ magnitude and B_1^+ phase respectively. The scan parameters used are displayed below:

- GRE (2D): TR=150 ms, TE=3 ms, flip angle=10 deg, slices=17x2 mm, imaging frequency 123.2583 MHz, resolution 192x192 pixels, FOV=30.72x30.72 cm
- SE (2D): TR=1000 ms, TE=15 ms, flip angle=90 deg, slices=17x2 mm, imaging frequency 123.2583 MHz, resolution 192x192 pixels, FOV=30.72x30.72 cm

Scan parameters were based on [28].

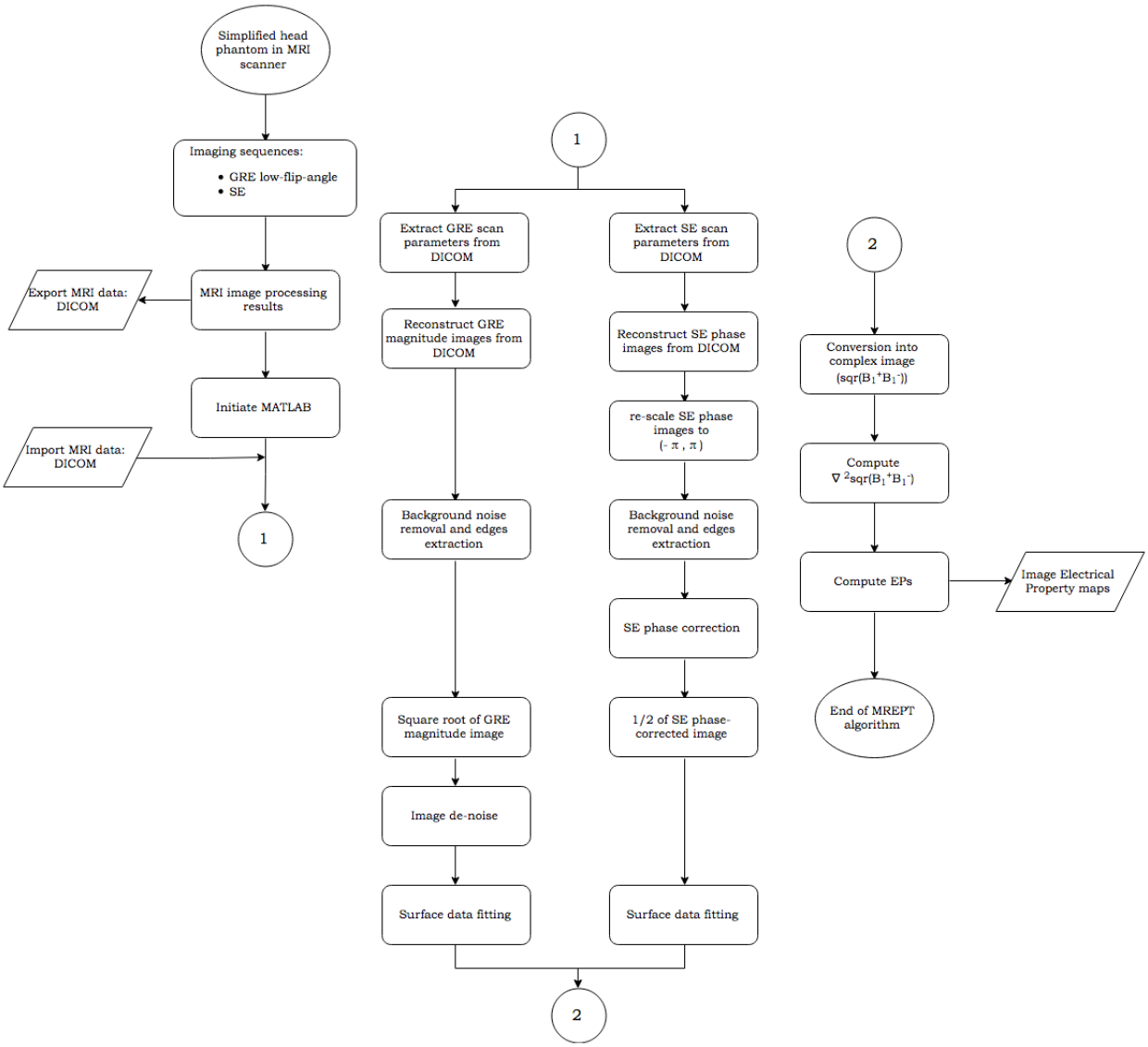

Figure 4: *MREPT's process flow diagram*

3.3.1 Image pre-processing

DICOM analysis

DICOM(Digital Imaging and Communications in Medicine), is the international standard for medical images. DICOMS are used in basically every medical imaging device for translating imaging information into electronic format that allows easy storage, deep computational analysis and easy exchanging between medical professionals and researchers around the world [35]. DICOM is the file format in which information was given by the MR scan that was made on the head phantom enabling it for further processing on a different platform. In our case, the platform chose is MATLAB (MathWorks, USA). The DICOM not only holds data related to the image, it also stores in a very detailed manner all scan parameters and all other relevant information related to it. In the header of the DICOM it is displayed information even about the institution in which the scanning took place and the technician that performed it. The scanning parameters shown before were not supplied by the institution, they were taken directly from the header. In Fig. 5 there's an example on how header information is displayed in MATLAB (MathWorks, USA).

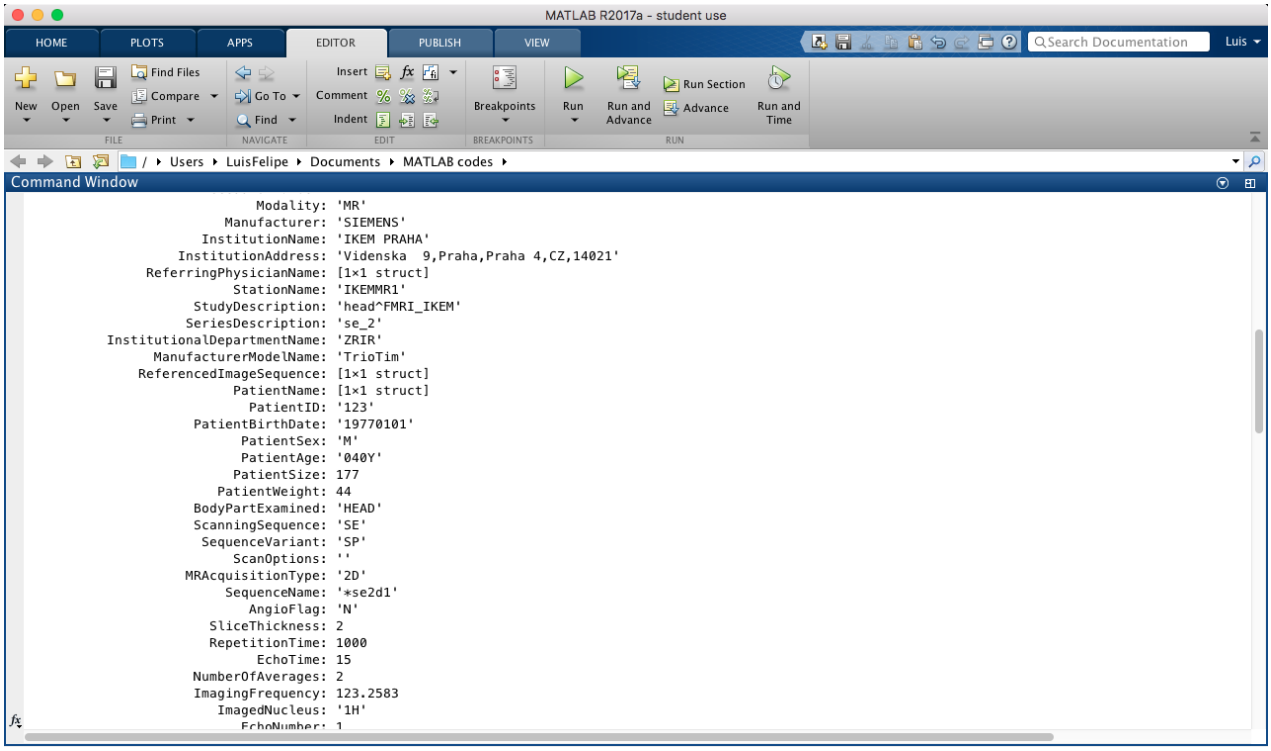

Figure 5: *Screenshot from the command window in MATLAB displaying information of the header of a DICOM*

Interpreting data in the header is not straight forward, for example, information about the units of scan parameters are missing. Detailed information about each item in the header can be easily looked up using official databases on the internet. For instance, let's

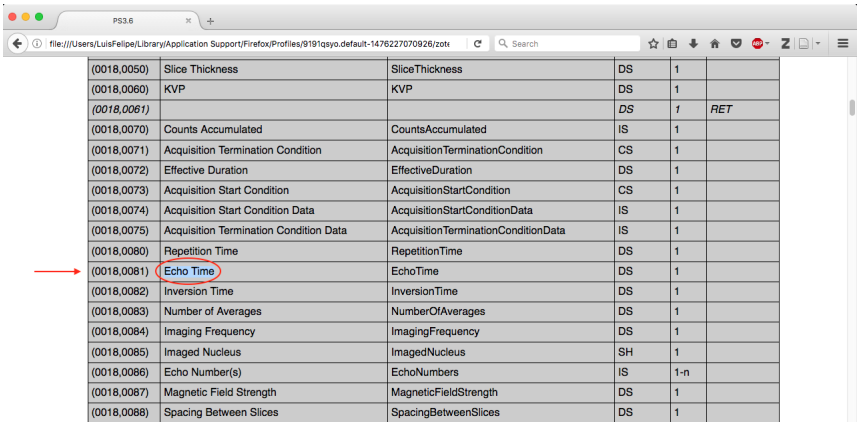

(0018,0050)	Slice Thickness	SliceThickness	DS	1	
(0018,0060)	KVP	KVP	DS	1	
(0018,0061)			*DS*	*1*	*RET*
(0018,0070)	Counts Accumulated	CountsAccumulated	IS	1	
(0018,0071)	Acquisition Termination Condition	AcquisitionTerminationCondition	CS	1	
(0018,0072)	Effective Duration	EffectiveDuration	DS	1	
(0018,0073)	Acquisition Start Condition	AcquisitionStartCondition	CS	1	
(0018,0074)	Acquisition Start Condition Data	AcquisitionStartConditionData	IS	1	
(0018,0075)	Acquisition Termination Condition Data	AcquisitionTerminationConditionData	IS	1	
(0018,0080)	Repetition Time	RepetitionTime	DS	1	
(0018,0081)	Echo Time	EchoTime	DS	1	
(0018,0082)	Inversion Time	InversionTime	DS	1	
(0018,0083)	Number of Averages	NumberOfAverages	DS	1	
(0018,0084)	Imaging Frequency	ImagingFrequency	DS	1	
(0018,0085)	Imaged Nucleus	ImagedNucleus	SH	1	
(0018,0086)	Echo Number(s)	EchoNumbers	IS	1-n	
(0018,0087)	Magnetic Field Strength	MagneticFieldStrength	DS	1	
(0018,0088)	Spacing Between Slices	SpacingBetweenSlices	DS	1	

(a)

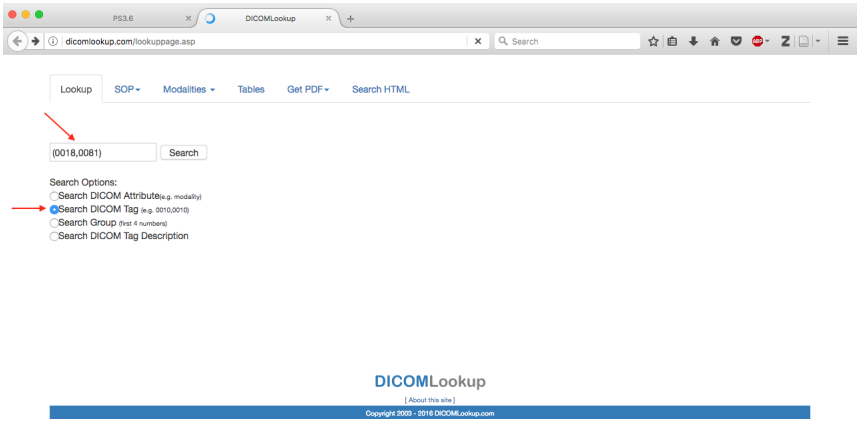

(b)

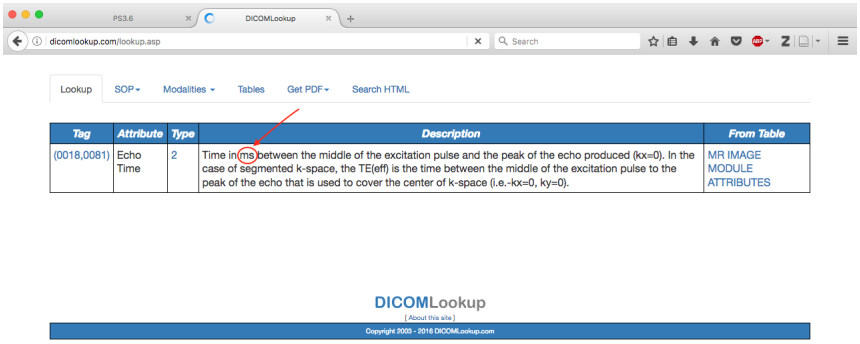

(c)

Figure 6: *Sequence for looking up information about specific attribute contained in a DICOM's header. a) Pointing to tag number of specific attribute in* [36]. *b) Searching attribute using tag number in* [37] *c) Display of attribute information*

say that the units of the number displayed under item EchoTime would like to be known. Search can be done of this name on [36](Fig. 6a). Notice on the left, every attribute holds a unique "Tag number". This tag number can be used to look up information regarding the particular attribute on [37](Fig. 6b and 6c). There it can be seen that the value shown on the header has units in milliseconds. This same process can be done for most of the items displayed on the header. The attributes relevant to MREPT processing in this work will be: Rows, Columns, PixelSpacing, ImagingFrequency, SliceThickness and SpacingBetweenSlices.

From the DICOM, GRE magnitude and SE phase images will be formed. SE phase image will be re-scaled to (-π, π), as SIEMENS outputs phase images with values $(0, 4096)$ with 2048 being the zero phase [38].

Images Clean-up

For a smooth EPT to take place, computation needs to be done over areas of constant electrical properties, that means an area in the image without abrupt changes in contrast. GRE magnitude and SE phase images will undergo an initial processing in which background data noise will be given value "0", and boundaries of the individual phantoms will be removed.

Phase Correction

Phase images coming from SE sequence might need additional processing as they may contain errors due to different reasons [9]. A proposal arises for a method for phase correction using the autocorrelation function and histograms [39]. This method is the one applied on this work.

Errors typically found on resulting phase images in nuclear magnetic resonance (NMR) include mis-adjustment of reference phase, a time lag in data acquisition, and different adding delays and disturbances added naturally by electronic filters. [39]

The two primary error terms found on distorted phase images will be referred as first-order($\epsilon_1 x$) and zero-order(ϕ_0) errors. The original phase image, coming directly from the SE scanning sequence, can be expressed as:

$$\hat{f}(x, y) = f(x, y) exp^{i\phi_0} exp^{i\epsilon_1 x}, \tag{41}$$

where $f(x, y)$ is the ideal image, and that which will be focused on acquiring. The other two exponential factors represent the two error terms mentioned above that will be needed

to eliminate. This method employs a two-step process, using first autocorrelation and then data redistribution using histograms, for estimating the two error terms. Once estimated, the error terms are eliminated by inverse multiplication.

For estimation of the first-order error ($\epsilon_1 x$), the autocorrelation of adjacent pixels in the x-direction in the distorted image $\hat{f}(x, y)$ is calculated.

$$\rho_x(y) = \mathrm{E}[f(x, y) f * (x + 1, y)] exp^{-\mathrm{i}\epsilon_1 x} \tag{42}$$

In (42), $\rho_x(y)$ is the expression for autocorrelation mentioned above, where E denotes expected value and ϵ_1 unit distance (pixel) phase error. For most NMR images the quantity enclosed by the E is positive real in general. Therefore, the first-order error term can easily be extracted by doing

$$\epsilon_1 = -phase[\rho_x(y)]. \tag{43}$$

When ϵ_1 is derived, an inverse multiplication is done on (41) to do the first-order phase correction:

$$\begin{aligned} \hat{f}(x, y) exp^{-\mathrm{i}\epsilon_1 x} &= f(x, y) exp^{\mathrm{i}\phi_0}, \\ \hat{f}_1(x, y) &= f(x, y) exp^{\mathrm{i}\phi_0}. \end{aligned} \tag{44}$$

$\hat{f}_1(x, y)$ is the resulting image after the first-order error correction. Only the zero-order error ϕ_0 offset now remains.

ϕ_0 offset is usually a delay caused in the electronic channels during acquisition. A phase histogram of the first-corrected image is used to estimate ϕ_0. According to used reference, as image comes from a SE imaging sequence, it is expected to find in the phase histogram that data is distributed around a particular value, this particular value is our ϕ_0.

Once again, by doing an inverse multiplication, the zero-order phase error term is eliminated, and a true SE phase image is finally obtained:

$$\hat{f}_1(x, y) e^{-i\phi_0} = f(x, y). \tag{45}$$

This is an easy-to-apply process that gives good results. If the reader is more interested in the background concepts regarding this method in [39] not only is the method explained but also applied on easy-to-follow different examples.

At this point, GRE magnitude image can be square-rooted, and SE phase-corrected image halved, in order to obtain $\sqrt{B_1^+ B_1^-}$ magnitude and $\sqrt{B_1^+ B_1^-}$ phase respectively.

Magnitude De-noising

Resultant $\sqrt{B_1^+ B_1^-}$ magnitude from square-rooted GRE scans present a lot of noise which unfortunately does not let a straight-forward operation for EPT to take place. Because it is dealt with images, it seemed that using conventional image filtering techniques would suffice. Methods like 2D convolutions using gaussian filtering or averaging kernels improved the image itself by making it clearer and smoother, but it also modified the waveform of the $\sqrt{B_1^+ B_1^-}$ field. Using normal imaging techniques may work well from improving appreciation of an image, but they did not satisfy the need for preserving core information. For this purpose, a more subtle approach that would be able to get rid of the noise while maintaining the proper waveform of the $\sqrt{B_1^+ B_1^-}$ field was needed. Enter image de-noising by use of the Wavelet Transform.

The Wavelet Transform is a process for frequency components estimation similar to the Fourier transform, different in that it does not use sinusoids infinite in time. Instead, it uses time-finite and frequency-varying waveforms to evaluate and extract different frequency components of the target wave [40].

$\sqrt{B_1^+ B_1^-}$ magnitude image will be processed by applying a de-noising built-in function from the Wavelet Toolbox in MATLAB (MathWorks, USA). This function uses a 5th level decomposition, "sym8" wavelet, with soft SureShrink thresholding technique [40].

2D fitting

Doing the Laplacian calculation through central difference equations has its drawbacks. On a noisy signal, second derivative calculations through central difference equations will only amplify the noise [41]. Images used on this work are not perfect examples of 2D wave propagation, noise is sure to be encountered and therefore artifacts will be introduced in the output image after EPT.

In order to have a more stable calculation of the Laplacian, the images underwent a second-order polynomial surface fitting (in $x-$ and $y-$direction). Our approach is similar to one research paper in which a parabola fitting was used in order to calculate electrical

conductivity for breast tumors [41].

3.3.2 EPs computation

As it has been stated, calculation of the Laplacian of $\sqrt{B_1^+ B_1^-}$ is the main problem in direct EPT calculation, as all other values are already given. For this calculation, a 2D-convolution kernel using the second-nearest neighbor was applied.

$$\nabla^2 B_1^+ = \frac{1}{4h^2} * \begin{bmatrix} 0 & 0 & 1 & 0 & 0 \\ 0 & 0 & 0 & 0 & 0 \\ 1 & 0 & -4 & 0 & 1 \\ 0 & 0 & 0 & 0 & 0 \\ 0 & 0 & 1 & 0 & 0 \end{bmatrix} \tag{46}$$

Where h is the distance between pixels' centers, which will be derived from the DICOM header. Using this approach is the same as using central difference equations in x and y-direction for second derivative estimation using second-nearest neighbor data point, and then summing them together to get the Laplacian. Using a 2D convolution function is far more efficient for the algorithm in MATLAB (MathWorks, USA).

For pixel-wise, relative permittivity and electrical conductivity computation of the phantoms, equations (26) and (27) were applied respectively. The values used for the rest of the terms in the equations were as follows:

$$\begin{aligned} \mu_0 &= 1.2566 \times 10^{-6} \quad \mathrm{H \cdot m^{-1}} \\ \varepsilon_0 &= 8.8542 \times 10^{-12} \quad \mathrm{F \cdot m^{-1}} \\ \omega &= 7.7445 \times 10^{8} \quad \mathrm{Rads \cdot s^{-1}} \end{aligned} \tag{47}$$

Please note that in this practical MREPT exercise we are only taking into account the two-dimensional space, differing from the three-dimensional approach in the simulations.

4 Results

4.1 Phantom creation

After mixing the different mentioned substances, three samples were obtained, with final EP values in good agreement with target values. Final relative permittivity and electrical conductivity for each sample, with its respective recipe are shown on Table 3.

Table 3: *Final composition of individual samples with correspondent electrical properties at 123 MHz*

Samples	H_20 (g)	Salt (g)	Isop (ml)	ε_r $(-)$	σ $\left(\mathrm{S}\cdot\mathrm{m}^{-1}\right)$
Hemorrhagic stroke	450	3,9	24	73,9	1,24
Ischemic stroke	270	1,25	180,3	47,8	0,17
White matter	315	2,8	180,2	53,4	0,34

Table 4: *Differences between target and obtained electrical properties of samples*

	ε_r $(-)$			σ $\left(\mathrm{S}\cdot\mathrm{m}^{-1}\right)$		
Samples	Target	Obtained	Diff.	Target	Obtained	Diff.
Hemorrhagic Stroke	74,6	73,9	0,9%	1,24	1,24	$\approx 0\%$
Ischemic Stroke	48,1	47,9	0,4%	0,17	0,17	$\approx 0\%$
White matter	53,7	53,5	0,4%	0,35	0,34	2,9%

Differences analysis on values of obtained EPs in comparison to target EP values can be seen on Table 4.

For data validity, dielectric probe took 6 series of 201 measurements in frequencies between 23 and 223 MHz for each sample. Statistical analysis was done on resulting EP values for frequency equal to 123 MHz. Expanded uncertainty U(x) with $\mathrm{k} = 2$ was calculated for each EP mean value on each sample. Data results are displayed on Table 5.

4.2 Simulations results

Virtual samples simulation

The results from the initial exercise of reconstruction of the original data vector were 210 slices of images with a field of view of 386 $\times$388 pixels. This volume represented magnetic field (B_1^+) distribution in all space within the birdcage coil. A center slice was taken and the complex image was decomposed into B_1^+ magnitude and B_1^+ phase (Fig. 7). The resulting relative permittivity and electrical conductivity maps can be seen on Fig. 8.

Table 5: *Data analysis of EP measurements with dielectric probe and network analyzer. Values of EPs from frequency at 123 MHz.* ε_r $(-)$, σ $\left(\mathrm{S}\cdot\mathrm{m}^{-1}\right)$.

	Hemorrhagic stroke		Ischemic stroke		White matter	
Series #	ε_r	σ	ε_r	σ	ε_r	σ
1	73,91	1,241	47,88	0,168	53,42	0,345
2	73,93	1,240	47,91	0,167	53,41	0,345
3	73,93	1,241	47,78	0,167	53,50	0,346
4	73,96	1,241	47,76	0,168	53,39	0,344
5	73,92	1,242	47,77	0,169	53,41	0,343
6	73,69	1,238	47,70	0,168	53,44	0,341
Mean	73,89	1,241	47,80	0,168	53,43	0,344
Std. dev.	0,092	0,001	0,071	0,001	0,033	0,002
U(x)	1,783	0,030	1,156	0,004	1,284	0,008

For each mapped phantom, all data points with relative permittivity values within $1< x<100$, and for electrical conductivity $0< x<4$, were statistically analyzed. Values outside of this ranges were discarded for any further processing as they are outside of the EPs values concerning brain tissues [9]. As it can be seen on Fig. 8, values of EPs vary in space, where contrast changes seem to increase towards the boundaries and seem to reduce towards the center. From the previous statistical analysis, a sample size was calculated for each phantom using (48), with a 95% level of confidence ($Z = 1,96$) and an error (err) of 0,5 for relative permittivity, and an error of 0,03 for electrical conductivity.

$$n = \frac{Z^2\sigma^2}{err^2} \tag{48}$$

Sample size (n) for each phantom varied depending on each phantom's data variance (σ^2). In Fig. 9 and Fig. 10 sample selection can be seen. Area of interest located near the center of sample, where changes in contrast appear to minimize. Table 6 and Table 7 show resultant mean values of EPs computation. Information considering initial statistical analysis can be found on Table 11 in Appendix B.

Head model

Data reconstruction gave output to a volume of 210 slices of 382 $\times$491 pixels images. The above mentioned statistical approach for analysis of results was not applied. Instead, a pixel from a center point within an area of interest was selected, and it's calculated EP values compared to literature values [34] at 128MHz. Electrical properties maps can be seen on Fig. 11, tissue classification on Fig. 12, and comparison between obtained values and literature on Table 8.

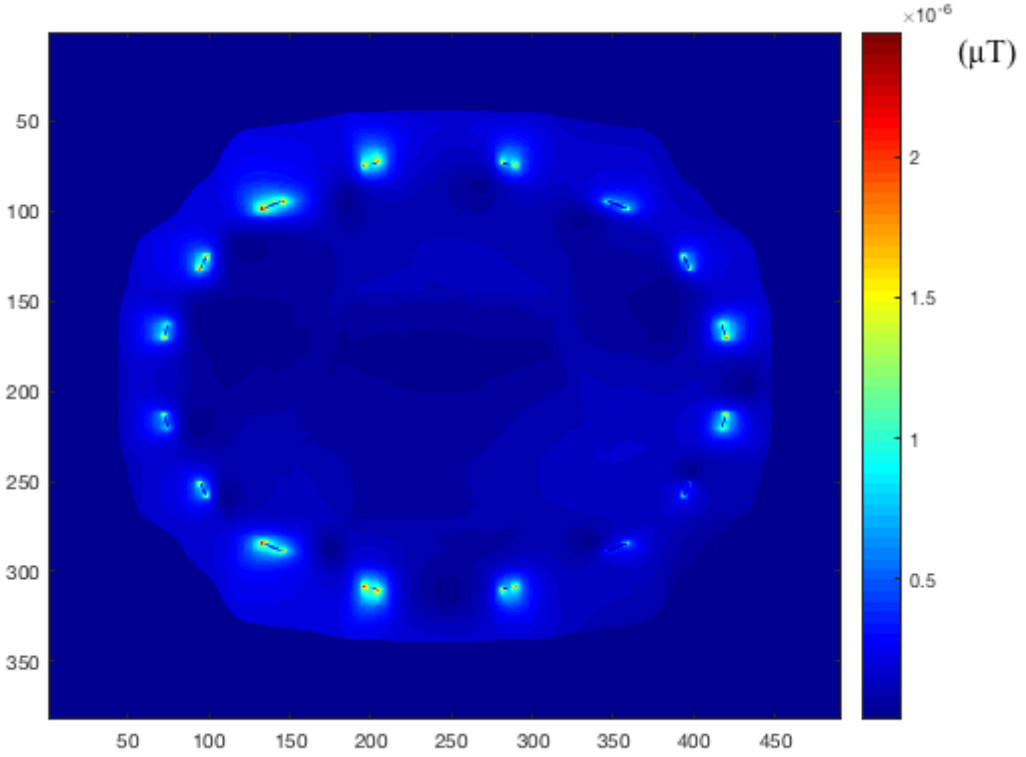

(a)

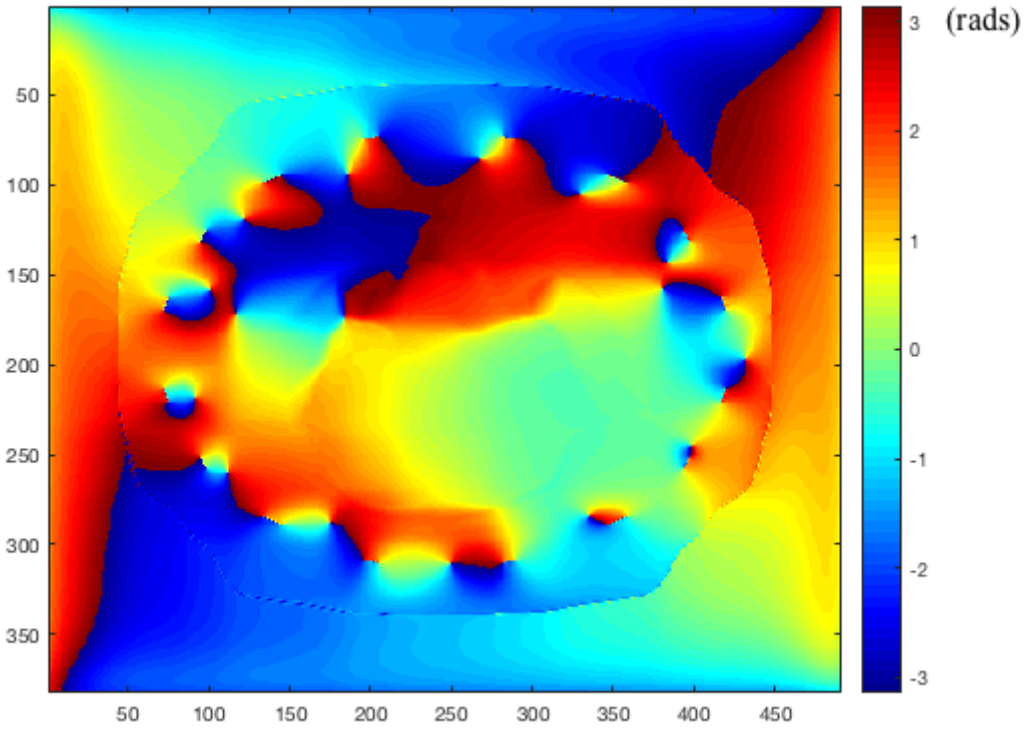

(b)

Figure 7: *B_1^+ complex data distribution from simulations a) B_1^+ magnitude, b) B_1^+ phase*

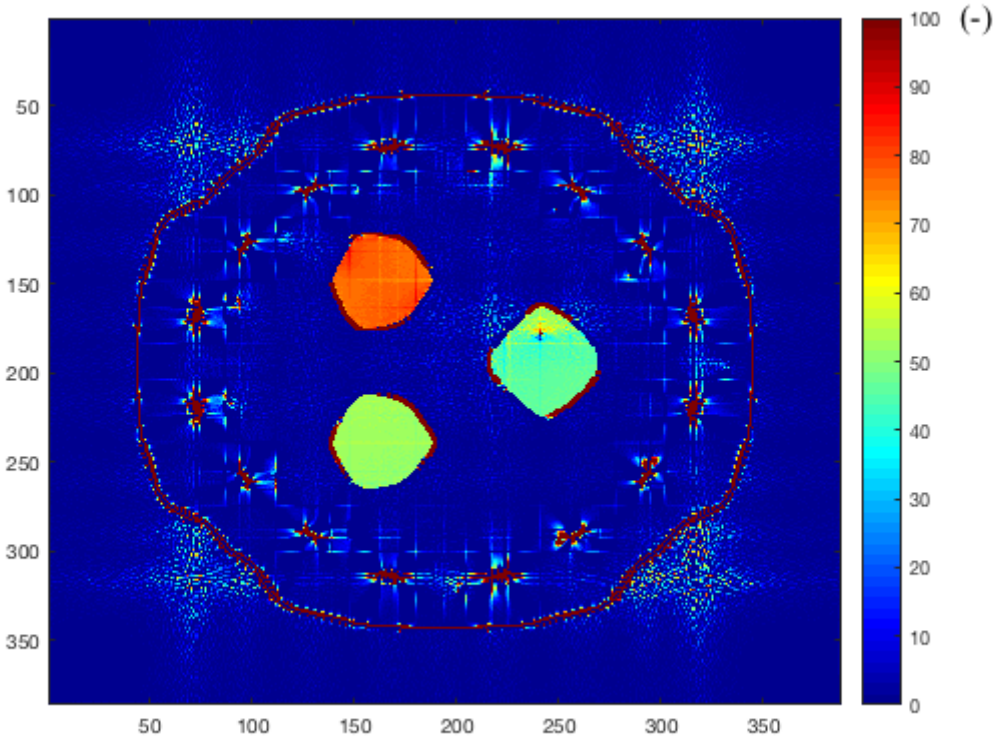

(a)

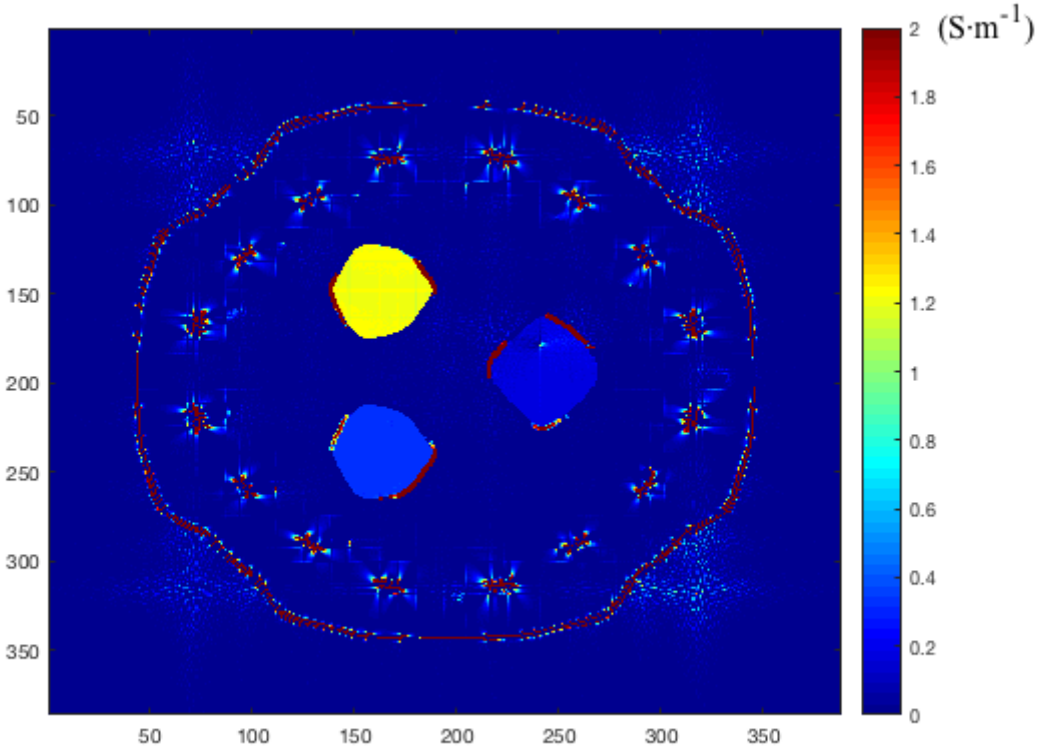

(b)

Figure 8: *Resulting electrical properties map of virtual samples a) ε_r map, b) σ map*

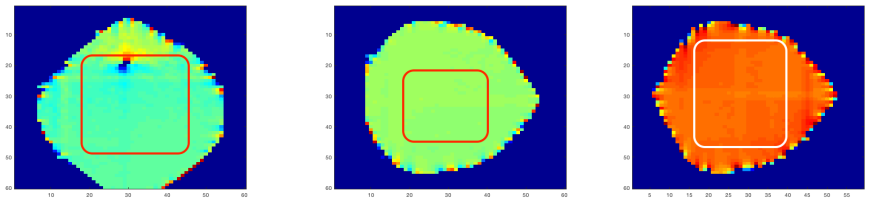

(a) (b) (c)

Figure 9: *Relative permittivity map of each virtual sample with selected region of interest for proper statistical analysis. a) Ischemic stroke, b) white matter, c) hemorrhagic stroke*

Table 6: *Estimation of relative permittivity of virtual samples based on statistical analysis within a region of interest far from the boundaries*

Virtual samples	ε_r $(-)$ real value	ε_r $(-)$ mean value	Variance (σ^2)	Std. dev.
hemorrhagic stroke	73,9	76,86	0,83	0,91
ischemic stroke	48,1	44,96	16,29	4,04
white matter	53,7	52,14	0,26	0,51

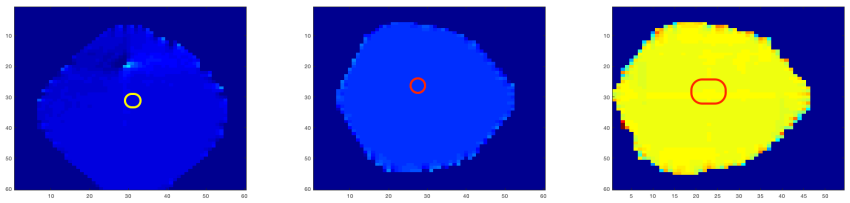

(a) (b) (c)

Figure 10: *Electrical conductivity map of each virtual sample with selected region of interest for proper statistical analysis. a) Ischemic stroke, b) white matter, c) hemorrhagic stroke*

Table 7: *Estimation of electrical conductivity of virtual samples based on statistical analysis within a region of interest far from the boundaries*

Virtual samples	σ $(-)$ real value	$\sigma(-)$ mean value	Variance (σ^2)	Std. dev.
hemorrhagic stroke	1,24	1,22	0,0000553	0,01
ischemic stroke	0,17	0,17	0,0000446	0,01
white matter	0,34	0,33	0,0000004	0,00

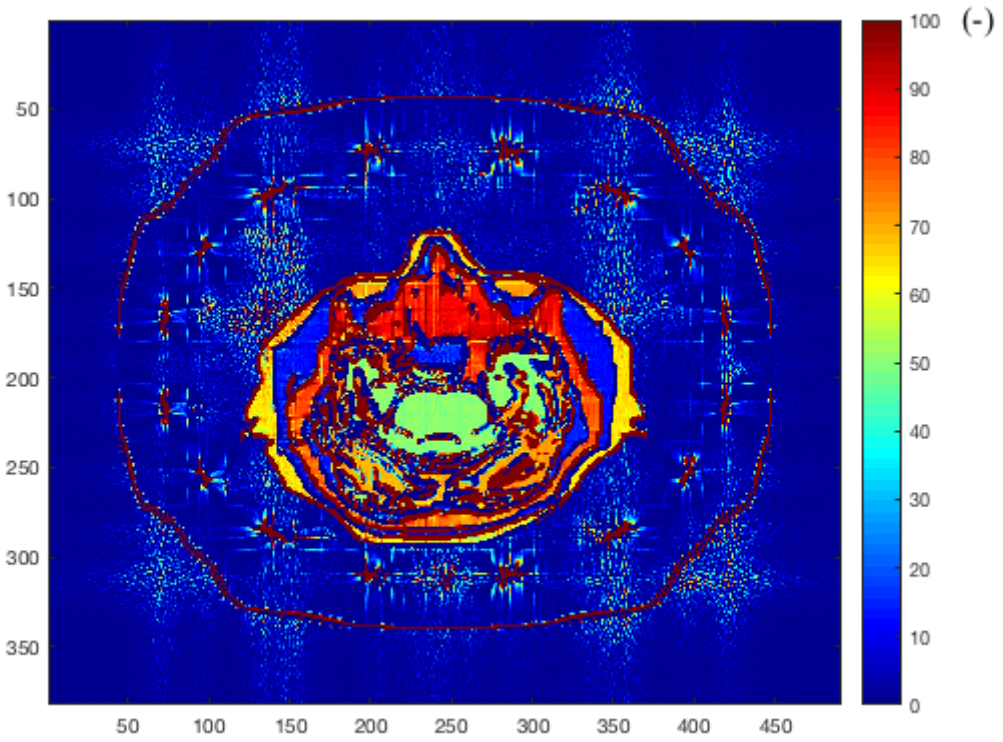

(a)

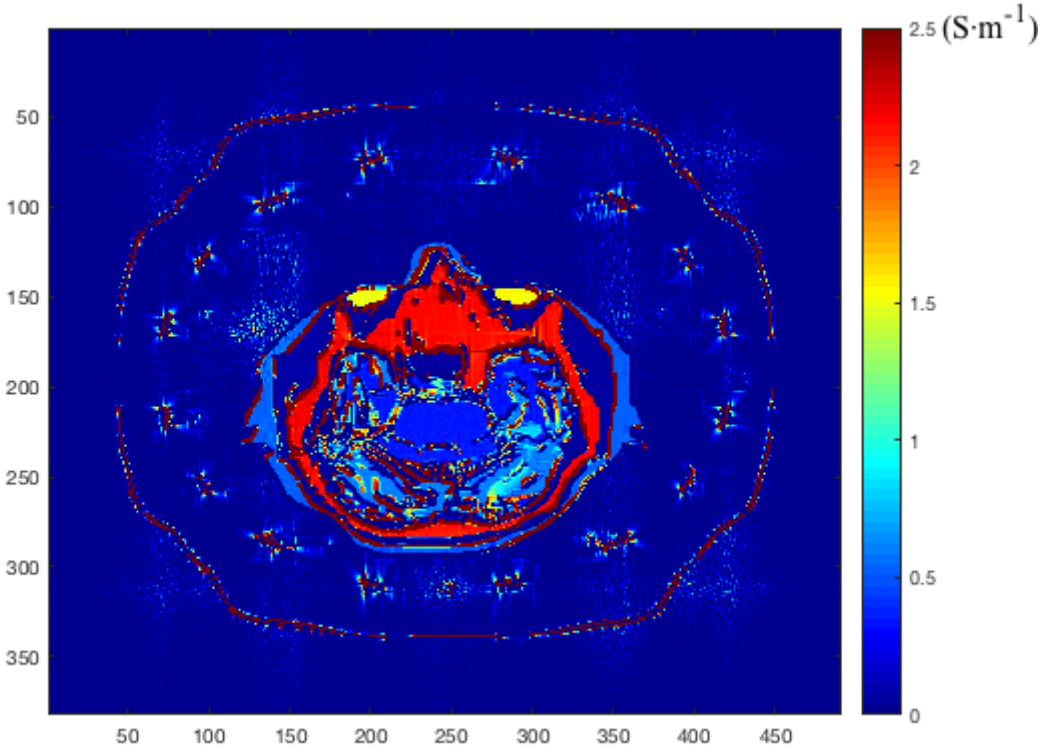

(b)

Figure 11: *Electrical Property mapping for real head model. a) ε_r map , b) σ map*

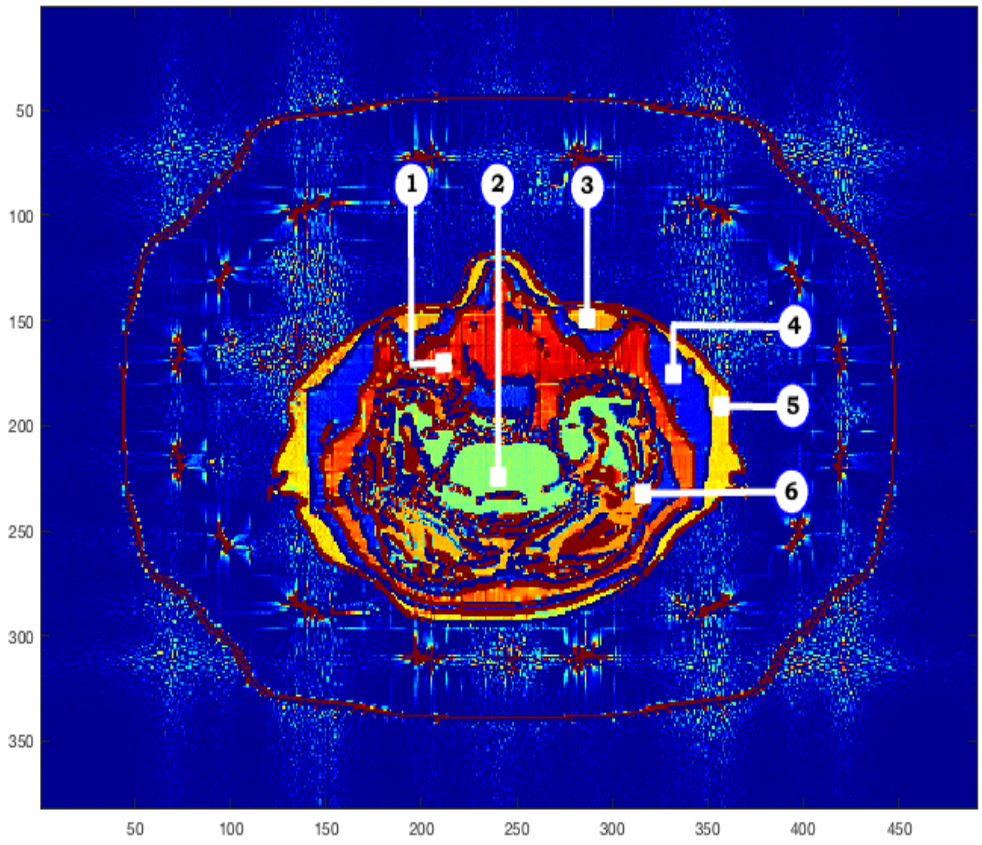

Figure 12: *Tissue classification of head model using ε_r map*

Table 8: *Comparison of measured EPs (meas.) and literature. Reference EPs (ref.) were taken at 128MHz from [34]. Measurement was done at exact location of markers shown on Fig 13.*

#	Tissue name	$\varepsilon_r(-)$ meas.	$\varepsilon_r(-)$ ref.	$\sigma(\mathrm{S}\cdot\mathrm{m}^{-1})$ meas.	$\sigma(\mathrm{S}\cdot\mathrm{m}^{-1})$ ref.
1	CSF	84,21	84,04	2,165	2,143
2	White matter	51,75	52,53	0,337	0,342
3	Eye (Vitreous Humor)	70,68	69,06	1,558	1,505
4	SAT	12,16	12,37	0,073	0,069
4	Bone (Cortical)	12,16	14,72	0,073	0,067
5	Skin	65,06	65,44	0,542	0,523
6	Gray matter	71,48	73,52	0,601	0,587

4.3 MREPT results

4.3.1 Image pre-processing results

DICOM analysis

From the DICOMS received, the MRI scan information for both GRE and SE, were reconstructed into two sets of 17 slices with 192 ×192 pixels field of view. Center slices from GRE magnitude and SE phase are shown on Fig. 13.

From the DICOM, other relevant information was also extracted:Rows, Columns, PixelSpacing, ImagingFrequency, SliceThickness and SpacingBetweenSlices.

Rows:	192	pixels
Columns:	192	pixels
Pixel Spacing:	0,0016	m
Imaging Frequency:	123,2583	MHz

It is important to note that MATLAB was not able to recognize the correct order of slices because of how they were named in the DICOM. Therefore, images had to be renamed.

Image clean-up

After clearing the background and removing the edges of the individual phantoms, new GRE magnitude and SE phase images result in what it is seen on Fig. 14 .

Phase correction

The cleared SE phase shown in Fig. 14b undergoes the phase correction method and yields the following values for inverse multiplication:

$$\epsilon_1 = \text{-0.0077}$$
$$\phi_0 = \text{-2.4}$$

The phase corrected image is displayed on Fig. 15. In Fig. 23 in Appendix C, from image Fig. 23a to Fig. 23b , progress of phase during correction is displayed using histograms. These histograms are placed on our work for reference in case the reader is interested in the phase correction method [39].

Mag de-noising

The GRE magnitude is square rooted in order to acquire an image which approximates to B_1^+ magnitude map (Fig. 16a). The surface of one individual phantom is extracted and imaged to show original noise (Fig. 16b). After the application of the de-noising wavelet

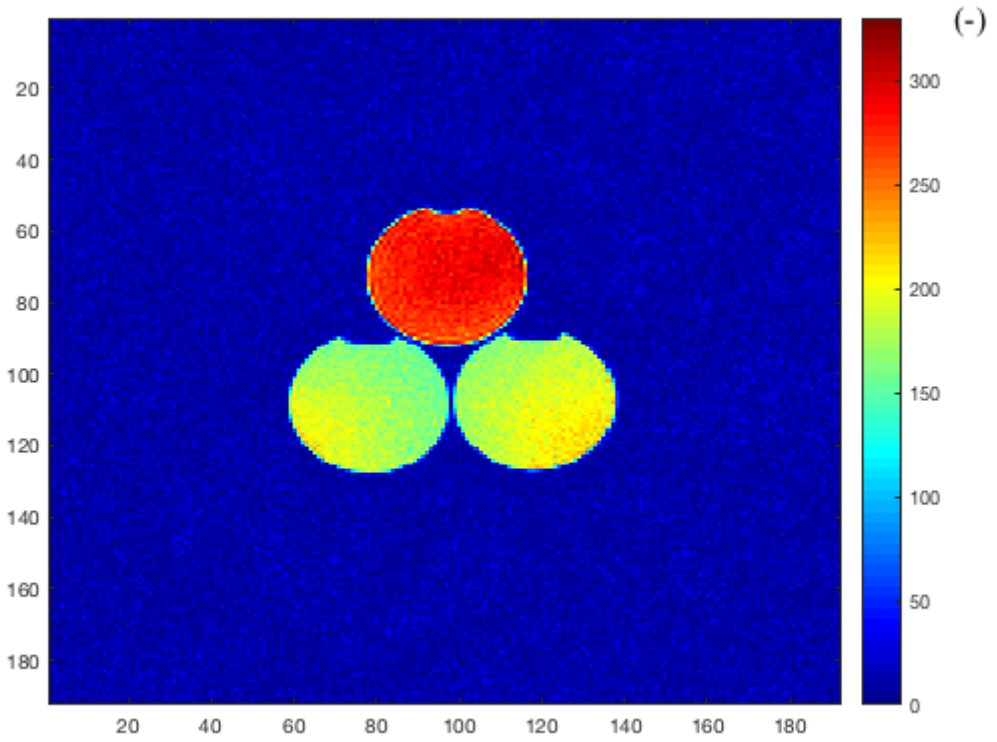

(a)

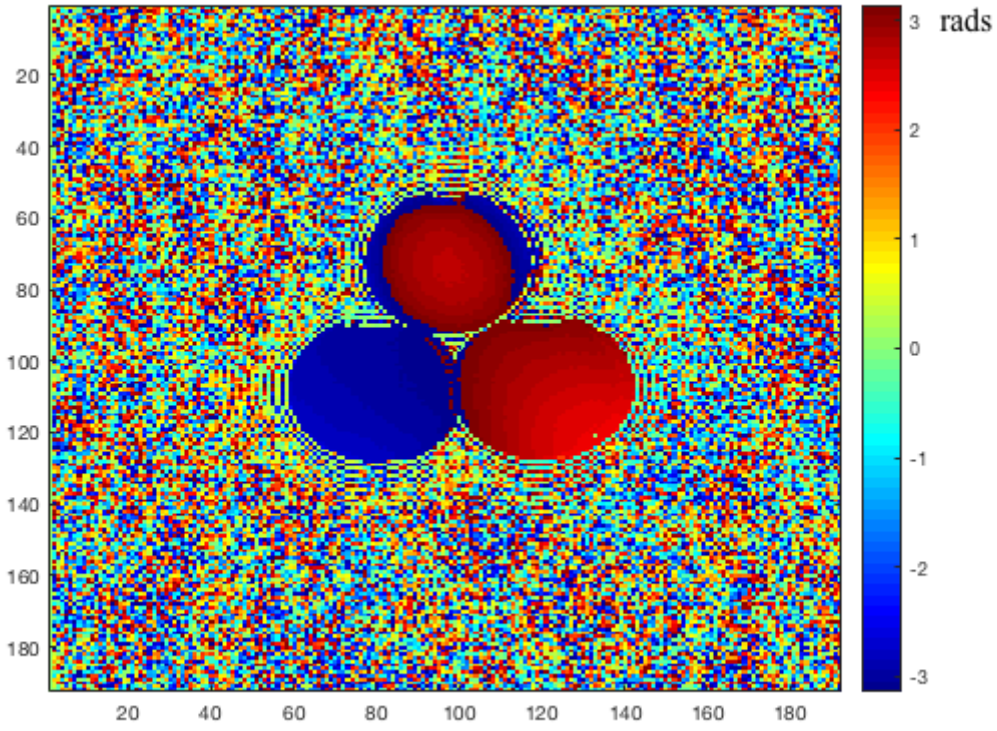

(b)

Figure 13: *Original images from MRI scan. a) GRE low-flip-angle magnitude image of a center slice b) SE phase image of a center slice*

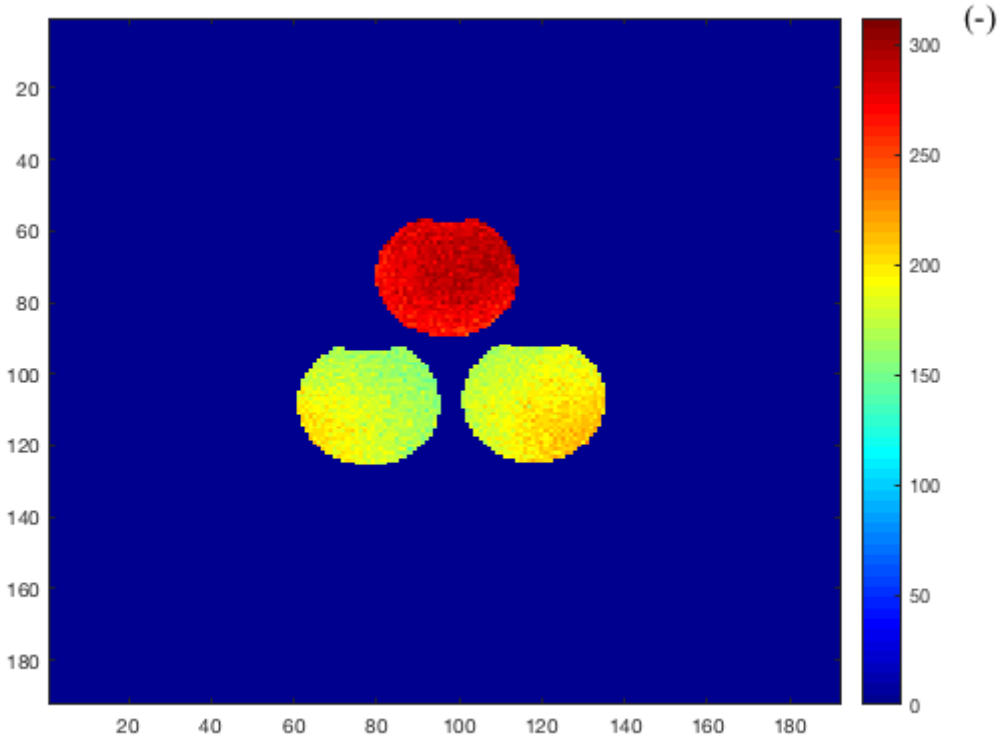

(a)

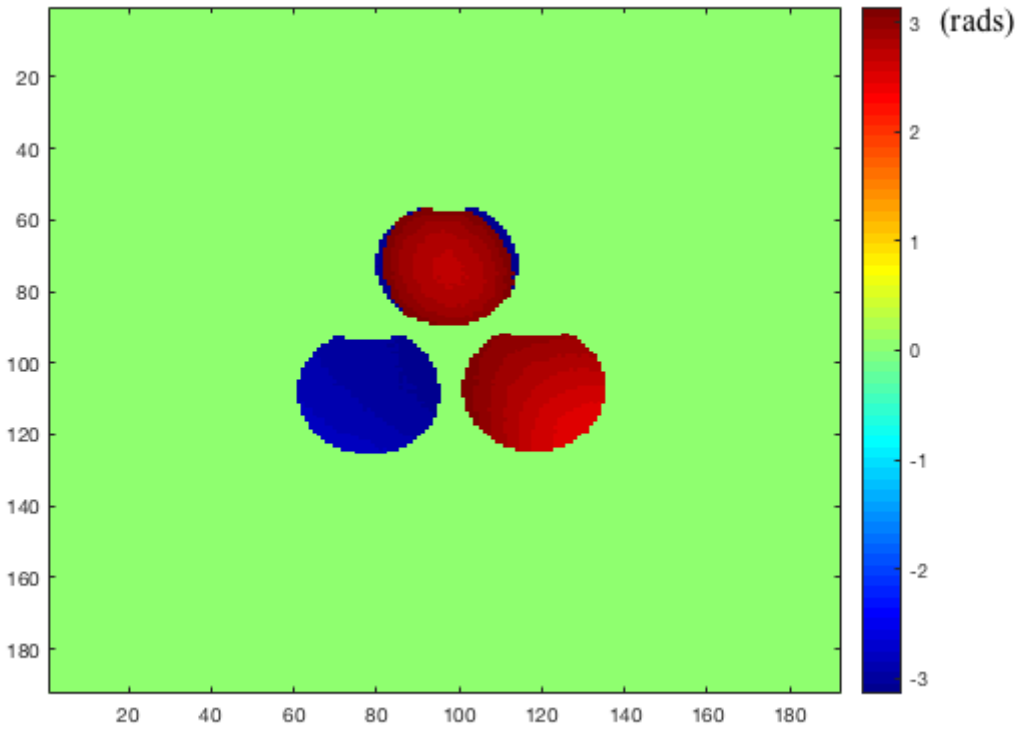

(b)

Figure 14: *Original images after processing for removal of background noise and edges of samples. a) GRE low-flip-angle magnitude image processed b) SE phase image processed*

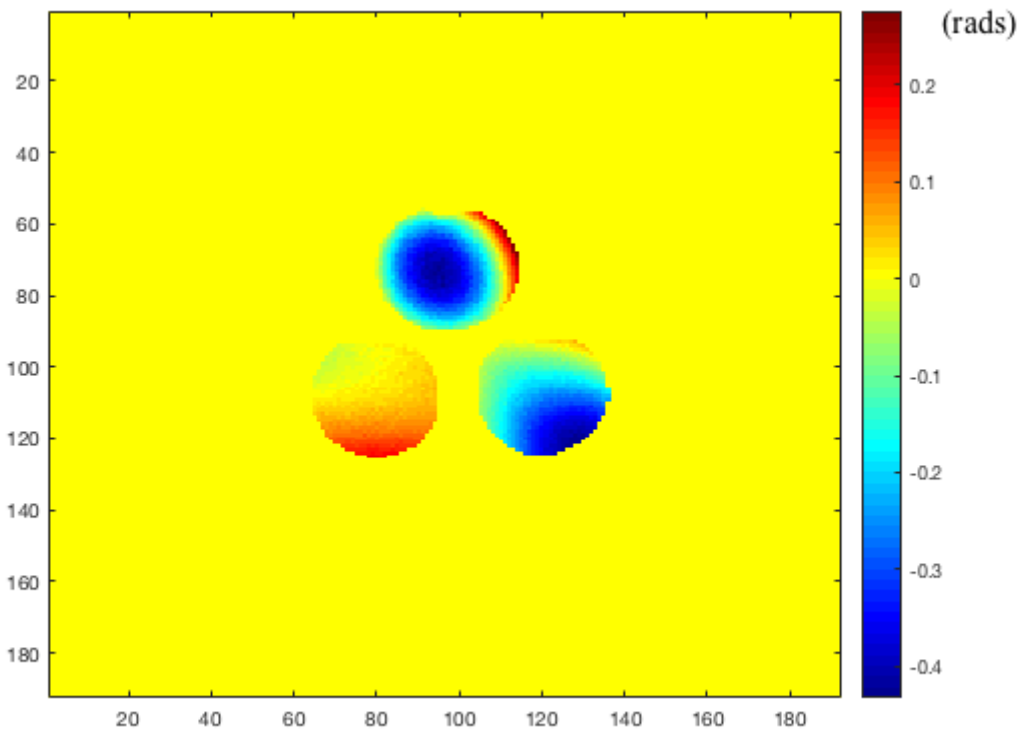

(a)

Figure 15: *SE phase corrected image*

transform function, the surface for each individual phantom are the ones shown on the left column on Fig. 17.

2D fitting

Second-order polynomial surface fitting of individual phantoms of square-rooted GRE de-noised images ($\sqrt{B_1^+ B_1^-}$ magnitude images), and halved SE phase-corrected images ($\sqrt{B_1^+ B_1^-}$ phase images) are displayed on Fig. 17 and Fig. 18.

4.3.2 EPs computation results

Each surface-fitted individual phantom is then reinserted in the original format image (Fig. 19) and $\sqrt{B_1^+ B_1^-}$magnitude and phase are joined to form one single complex-valued matrix. This image is convoluted using (46) and $\nabla^2\sqrt{B_1^+ B_1^-}$ is acquired and substituted in (26) and (27).

The resultant EP maps from the MREPT method are shown on Fig. 20. The same method for statistical analysis explained for the simulations is used here. Sample sizes are determined using (47) and relevant parameter and other statistical data of interest can be

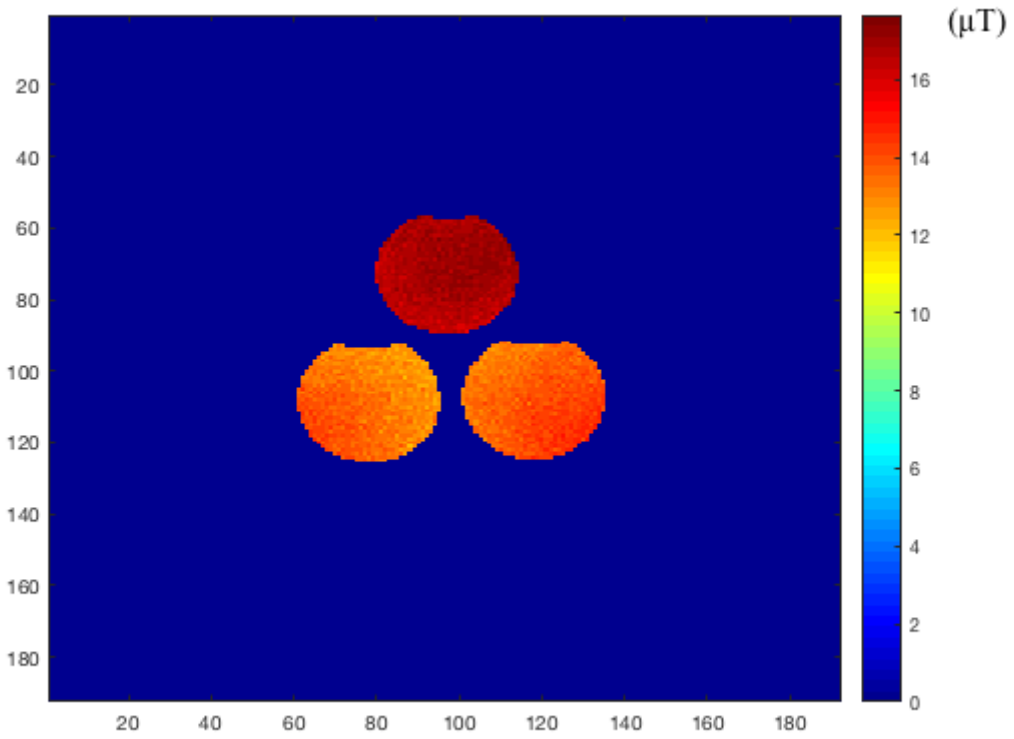

(a)

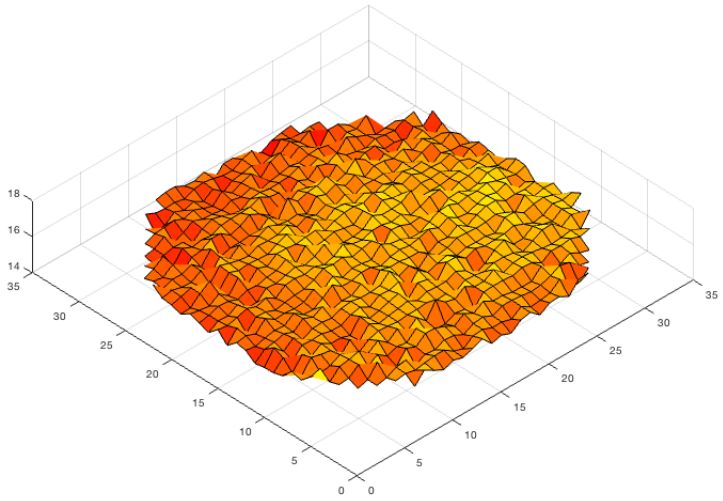

(b)

Figure 16: *Square-root of GRE low-flip-angle magnitude image a)* $\sqrt{B_1^+ B_1^-}$ *magnitude map of real samples b) Demonstration of noisy surface from top-center phantom on* $\sqrt{B_1^+ B_1^-}$ *magnitude map*

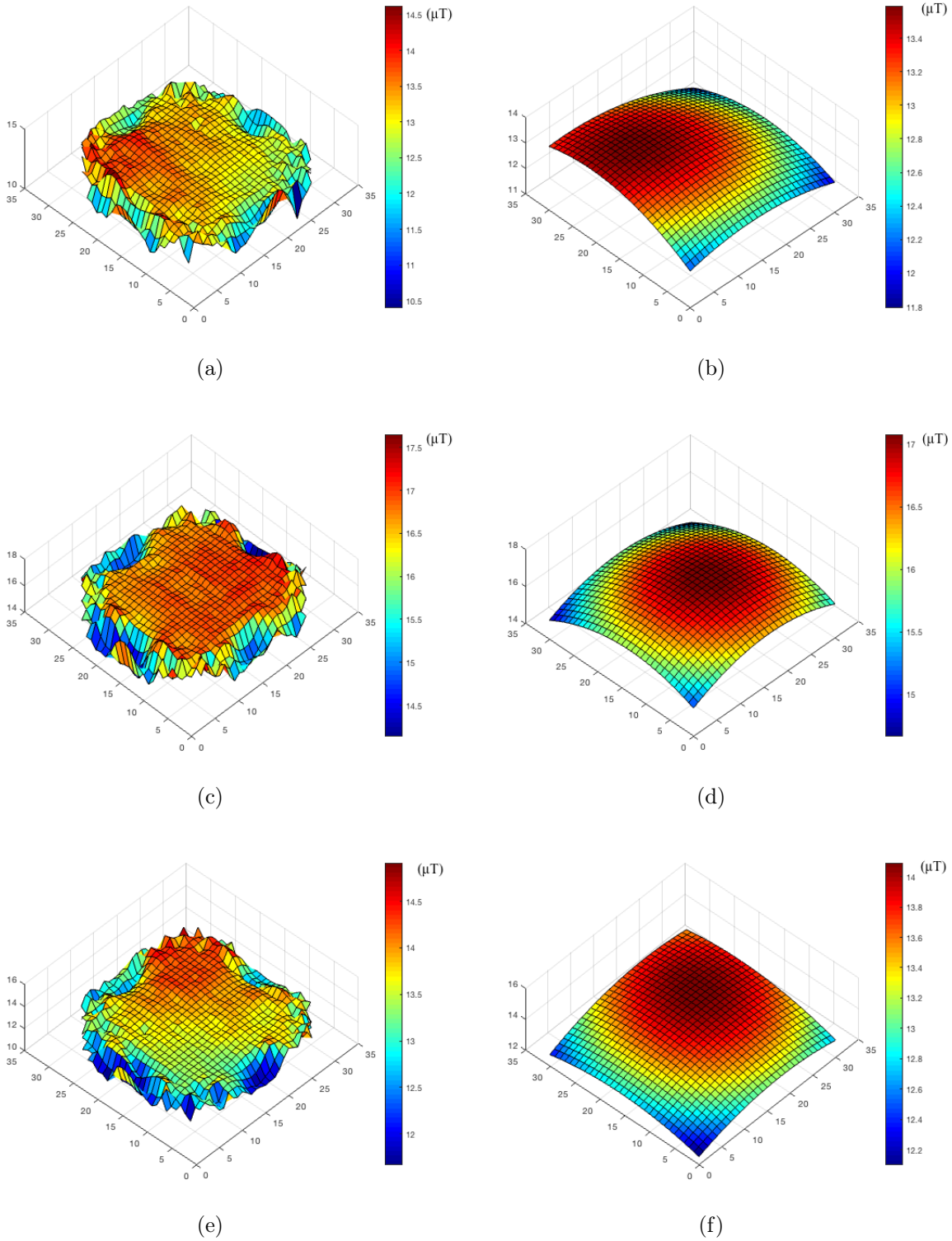

Figure 17: *Surface fitting* $\sqrt{B_1^+ B_1^-}$ *magnitude. a) Bottom left de-noised sample image, b) Bottom left de-noised sample surface fit, c) top center de-noised sample image, d) top center de-noised sample surface fit, e) Bottom right de-noised sample image f) Bottom right de-noised sample surface fit*

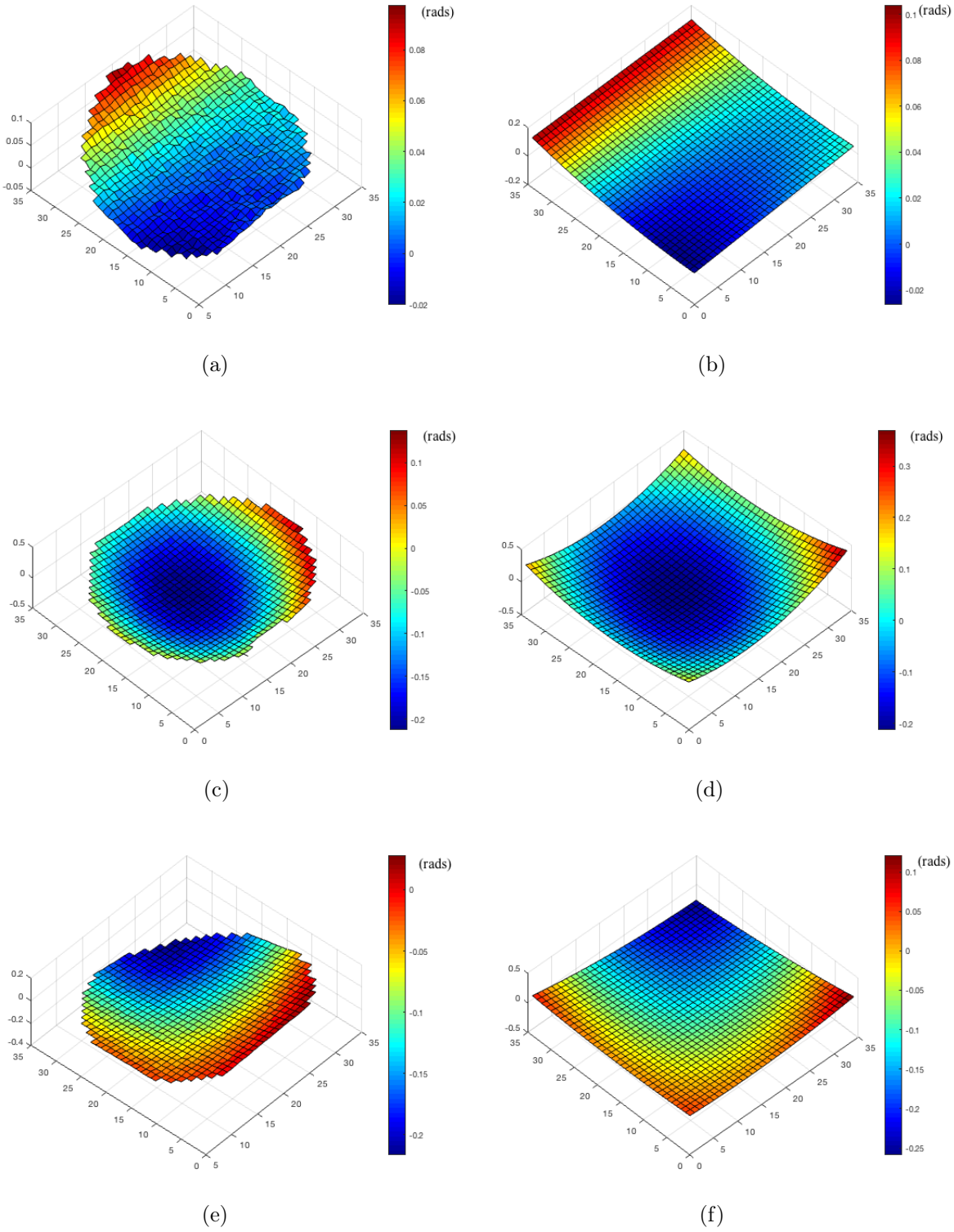

Figure 18: *Surface fitting* $\sqrt{B_1^+ B_1^-}$ *phase. a) Bottom left sample image, b) Bottom left sample surface fit, c) top center sample image, d) top center sample surface fit, e) Bottom right sample image f) Bottom right sample surface fit*

seen on Table 12 in Appendix B. Sample-area selection images and results are displayed on Fig. 21 and Fig. 22, Table 9 and Table 10. Values discarded and not computed if out of ranges $1 < x < 100$ for ε_r, and $0 < x < 2$ for σ.

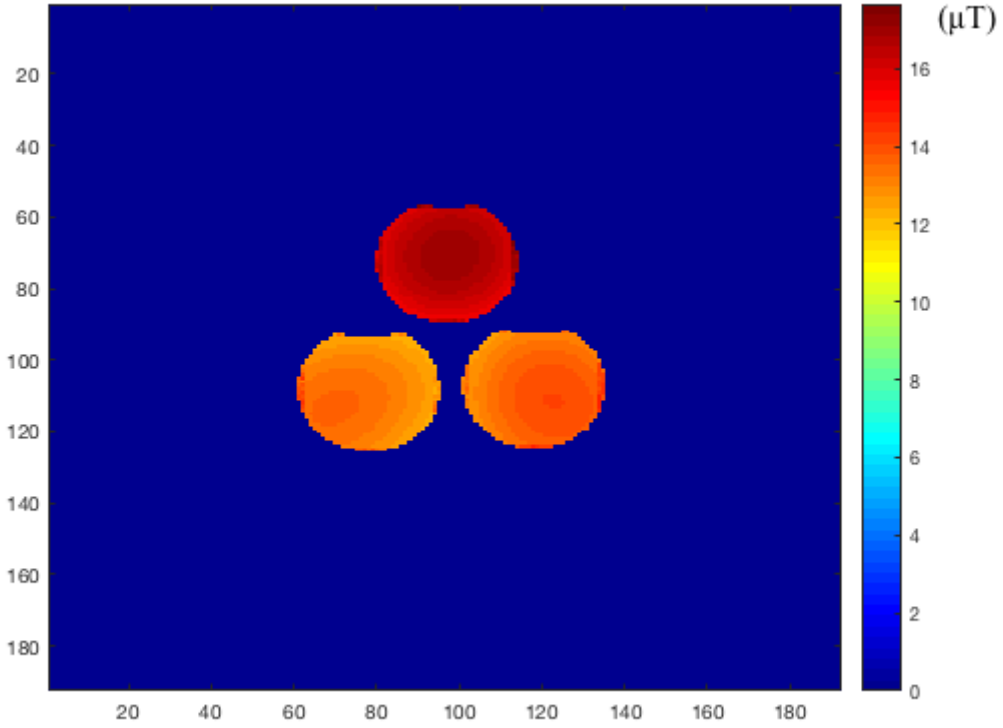

(a)

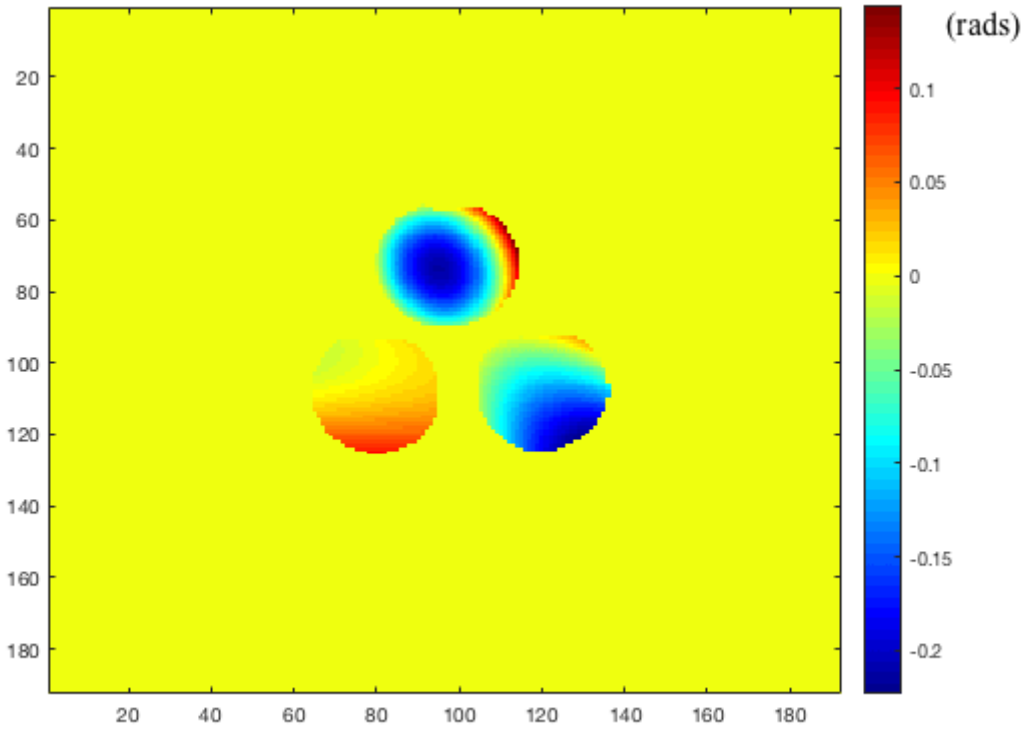

(b)

Figure 19: *Final images for complex* $\sqrt{B_1^+ B_1^-}$ *(eq. 30) a)* $\sqrt{|\,GRE\,|}$ *de-noised image (surface fitted) b)* $\frac{1}{2}SE$ *phase-corrected image (surface fitted)*

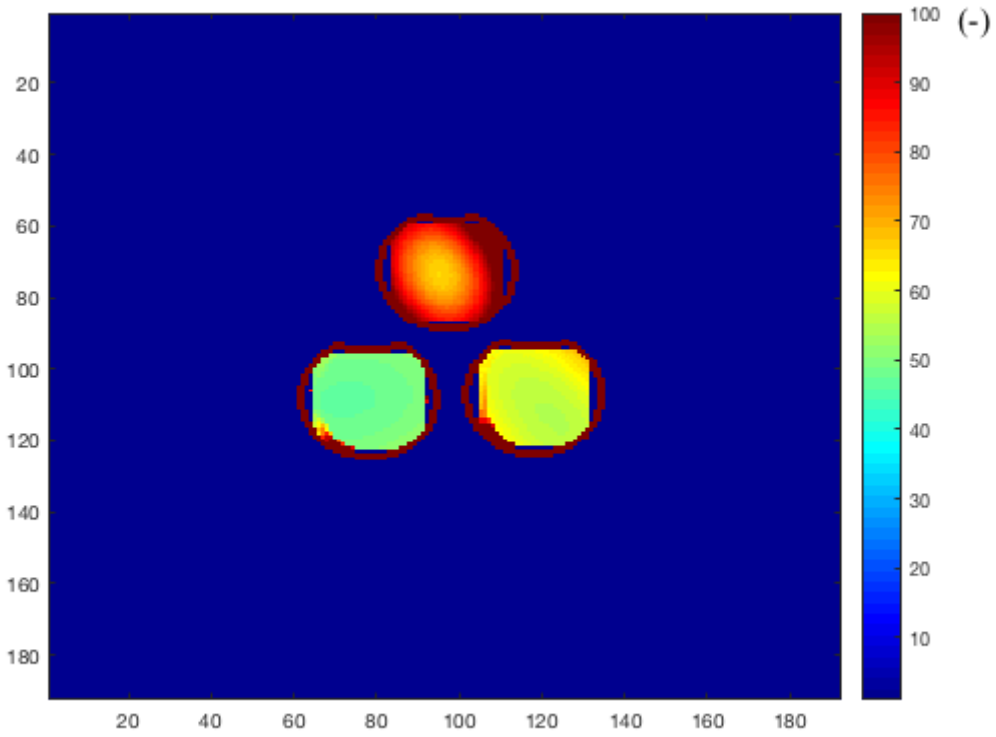

(a)

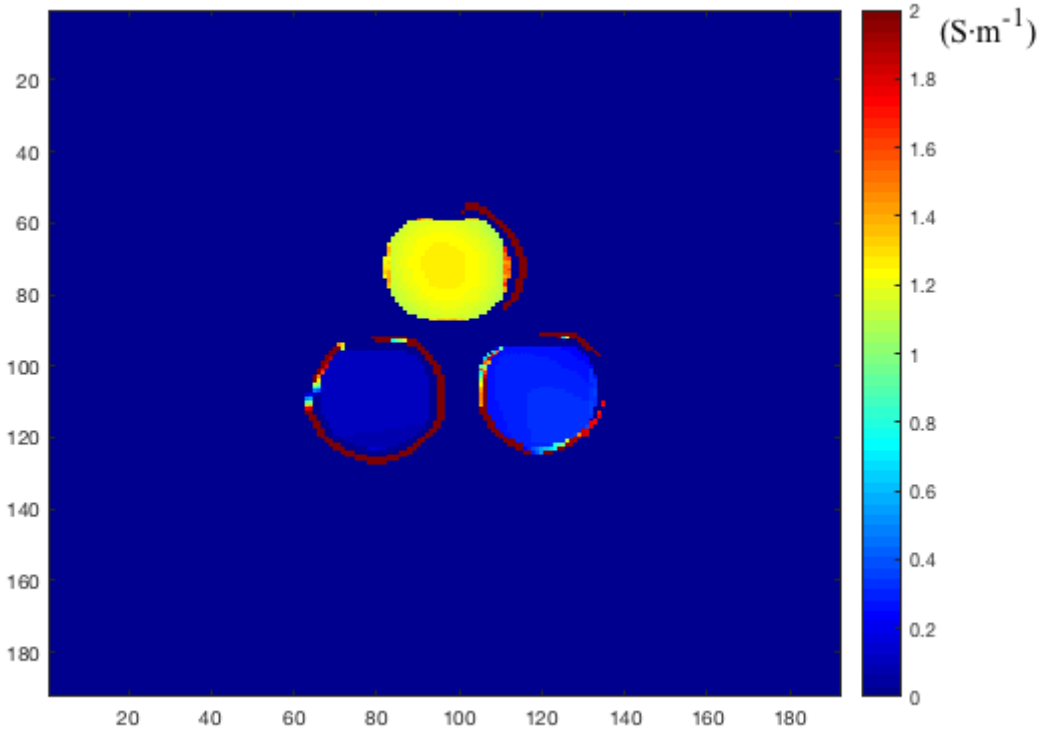

(b)

Figure 20: *Electrical property maps for samples within simplified head phantom using MREPT. a) ε_r map, b) σ map*

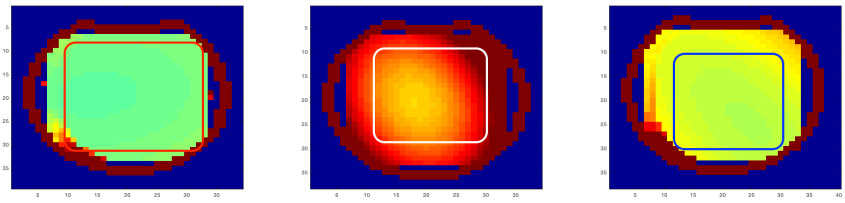

(a) (b) (c)

Figure 21: *Relative permittivity map of each real sample with selected region of interest for proper statistical analysis. a) Ischemic stroke, b) hemorrhagic stroke, c) white matter*

Table 9: *Estimation of relative permittivity of real samples based on statistical analysis within a region of interest far from the boundaries*

Real samples	ε_r $(-)$ real value	ε_r $(-)$ mean value	Variance (σ^2)	Std. dev.
hemorrhagic stroke	73,9	75,52	55,90	7,48
ischemic stroke	48,1	48,34	5,96	2,44
white matter	53,7	56,63	2,13	1,46

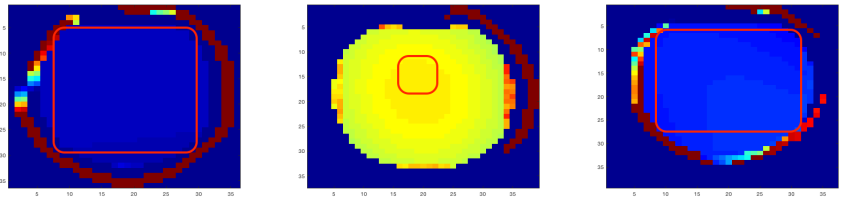

(a) (b) (c)

Figure 22: *Electrical conductivity map of each real sample with selected region of interest for proper statistical analysis. a) Ischemic stroke, b) hemorrhagic stroke, c) white matter*

Table 10: *Estimation of electrical conductivity of real samples based on statistical analysis within a region of interest far from the boundaries*

Real samples	σ $(-)$ real value	$\sigma(-)$ mean value	Variance (σ^2)	Std. dev.
hemorrhagic stroke	1,24	1,27	0,00	0,02
ischemic stroke	0,17	0,11	0,00	0,01
white matter	0,34	0,30	0,00	0,02

5 Discussion

The samples manufactured, for mimicking a very simple head phantom, served their purpose for this thesis. Initially it was a concern that perhaps the arrangement did not satisfy the symmetry conditions for magnetic field phase estimation, so perhaps in future studies, an even more simple phantom should be used in the MRI scanner in order to guarantee good results for research and analysis.

Results from simulations are in good agreement with expected outcome based on previous research and literature. Even though computation of $\nabla^2 B_1^+$ presented a challenge due to uneven data point distribution in B_1^+ raw maps, the in this thesis proposed derived modified central equation for second derivative was satisfactory. Once $\nabla^2 B_1^+$ map was established, estimating EPs from the Helmholtz equation was very much straight-forward. EP mapping results were satisfactory enough to create contrast between the different samples, and also provide EP values, close enough to real ones, in order to allow classification. Artifacts at the boundaries are observed. These are magnified when a pixel outside of the area of interest is used for computation of the second derivatives. Also, wave propagation is unstable at, or near the boundaries of the samples, therefore resulting in EP values with a larger deviation from the mean. Values for relative permittivity have higher standard deviations than those from electrical conductivity. A possible explanation could be that B_1^+ magnitude values are more likely to rapidly change, during EM wave propagation in space, than those of the phase. Relative permittivity is highly dependent on B_1^+ magnitude, just as electrical conductivity is dependent on B_1^+ phase [9]. Resulting EPs were expected to deviate from real sample EP values as they were aimed for a frequency of 123 MHz and simulations were done using a frequency of 128 MHz. However, the changes within this frequency band are not significant.

For the head model, the objective was to verify the extent of the designed algorithm when used to map more complex structures. As it can be seen from Fig. 12 and Table 8, 5 different tissues were correctly identified. Bone (cortical) and subcutaneous fat (SAT) were not correctly discriminated. These two type of tissues have very similar electrical properties therefore they are seen on Fig. 12 as if they were only one. They are blended because the algorithm is not accurate enough to be able to classify tissues with such small differences in EPs. It is found then a limitation in the method, as it proves not satisfactory to all tissue types.

For the MREPT method, every step taken in this work was absolutely necessary in order to achieve the reported results. It is understandable and expected that working with real data would prove to be more difficult than working with synthetic data, where

the experiment takes place in a virtually ideally-controlled environment. However, the challenge was actually greater as none of the reviewed research studies gave much importance to image processing prior to EP computations. In our work it was indeed the most significant obstacle towards these results. Results for the MRI scanned simplified head phantom were satisfactory in terms of mapping and classification. Even though results have a higher deviation from mean values than those from simulations, it is possible to correctly identify each sample within the image, for both, relative permittivity and electrical conductivity maps.

For EPs mean value calculations, size of the area of interest within every sample differed considerably for simulations and the MREPT exercise. Lower resolution and increased data variance affected the EPT, specifically the Laplacian computation. Even though, results of MREPT from MRI scans and numerical simulations did not differ considerably. Perhaps when working with more complex and smaller structures, the higher resolution offered in the simulations will mark a significant difference. In fact, no studies reviewed for this work showed an EP map of a real head as accurate and/or better looking as the ones shown in Fig. 12. The problem with resolution is that in an MRI image, different tissue types could be contained inside the same pixel, making EPT impossible with the approach used in our work. The major focus on recent research regarding MREPT lies on different mathematical approaches in order to overcome the problem with boundary artifacts, specially during the calculation of the Laplacian. Two examples of good methods considered during this work can be reviewed by the reader on [28] and [41].

In general, errors in EPs computation increases as one gets closer to a boundary. The use of a kernel for discrete numerical computation of second derivative, will eventually have edge pixels outside the tissue of interest, and therefore introduce an artifact in the estimated map. Also, EM wave won't behave properly as it interacts with encountered boundaries, only stable wave propagation in a medium of constant electrical properties will satisfy the Helmholtz equation and therefore only then can relative permittivity and electrical conductivity be derived with this method.

For all unhealthy tissue that have significant changes in EPs in comparison to its own on healthy state, EPT holds great potential in detection and classification, as well as in monitoring its behavior in time. In the case of strokes, results on this work give MREPT qualities to be potentially used for stroke detection and classification, but more research is necessary as strokes' EP values are widely variant depending on many factors, like type and time from onset of lesion. MREPT can be accurate when mapping events like breast malignant tissues [41], however it still needs to be improved if it is wanted to detect and classify problems within more complex body structures like the brain.

6 Conclusion

Three liquid samples, with relative permittivity and electrical conductivity of hemorrhagic stroke, ischemic stroke and white matter respectively, were created. The liquid samples were poured inside plastic recipients and assembled within a thin plastic bag in order to mimic a simplified head phantom. The head phantom underwent and MRI scan with GRE low-flip-angle and SE sequences for acquisition of magnetic field maps. EPT method applied using simulated B_1^+ data supplied satisfactory results for EPs mapping of virtually created individual strokes and tissue samples. For the head model it showed limitations when attempting to map tissues with little difference in electrical properties. EPT method applied from data extracted from MR images (MREPT), delivered satisfactory results for identification of samples for both, relative permittivity map and electrical conductivity map. Calculation of the Laplacian of the magnetic field distribution (B_1^+) is of great concern in past, current and near future research, as it introduces artifacts in resulting images.

References

[1] W. T. Joines, Y. Zhang, C. Li, and R. L. Jirtle, "The measured electrical properties of normal and malignant human tissues from 50 to 900 MHz," *Medical Physics*, vol. 21, no. 4, pp. 547–550, Apr. 1994. [Online]. Available: http://onlinelibrary.wiley.com/doi/10.1118/1.597312/abstract

[2] S. Y. Semenov, R. H. Svenson, V. G. Posukh, A. G. Nazarov, Y. E. Sizov, A. E. Bulyshev, A. E. Souvorov, W. Chen, J. Kasell, and G. P. Tatsis, "Dielectrical spectroscopy of canine myocardium during acute ischemia and hypoxia at frequency spectrum from 100 kHz to 6 GHz," *IEEE Transactions on Medical Imaging*, vol. 21, no. 6, pp. 703–707, Jun. 2002.

[3] E. M. Haacke, L. S. Petropoulos, E. W. Nilges, and D. H. Wu, "Extraction of conductivity and permittivity using magnetic resonance imaging," *Physics in Medicine and Biology*, vol. 36, no. 6, p. 723, Jun. 1991. [Online]. Available: http://80.iopscience.iop.org.dialog.cvut.cz/article/10.1088/0031-9155/36/6/002/meta

[4] A. L. van Lier, D. O. Brunner, K. P. Pruessmann, D. W. Klomp, P. R. Luijten, J. J. Lagendijk, and C. A. van den Berg, "B1+Phase mapping at 7 T and its application for in vivo electrical conductivity mapping," *Magnetic Resonance in Medicine*, vol. 67, no. 2, pp. 552–561, Feb. 2012. [Online]. Available: http://onlinelibrary.wiley.com/doi/10.1002/mrm.22995/abstract

[5] K. Balanis, "Advanced engineering in electromagnetics," United States, 1989.

[6] D. Miklavcic, N. Pavselj, and F. X. Hart, *Electric Properties of Tissues*. John Wiley & Sons, Inc., 2006. [Online]. Available: http://dx.doi.org/10.1002/9780471740360.ebs0403

[7] "IEEE Standard Definitions of Terms for Radio Wave Propagation," *IEEE Std 211-1997*, pp. i–, 1998.

[8] U. Katscher, D.-H. Kim, and J. K. Seo, "Recent Progress and Future Challenges in MR Electric Properties Tomography," *Computational and Mathematical Methods in Medicine*, vol. 2013, pp. 1–11, 2013. [Online]. Available: http://www.hindawi.com/journals/cmmm/2013/546562/

[9] S. B. Bulumulla, S. K. Lee, and D. T. B. Yeo, "Conductivity and permittivity imaging at 3.0t," *Concepts in magnetic resonance. Part B, Magnetic resonance engineering*, vol. 41B, no. 1, pp. 13–21, Feb. 2012. [Online]. Available: http://www.ncbi.nlm.nih.gov/pmc/articles/PMC3627401/

[10] U. Katscher, H. Abe, M. K. Ivancevic, K. Djamshidi, P. Karkowski, and G. M. Newstead, "Towards the Investigation of Breast Tumor Malignancy Via Electric Conductivity Measurement," *ISMRM (International Society Magnetic Resonance in Medicine)*, vol. 21, p. 3372, Apr. 2013. [Online]. Available: http://dev.ismrm.org/2013/3372.html

[11] E. Balidemaj, *MR based electric properties imaging for hyperthermia treatment planning and MR safety purposes.* 9789402801651, 2016. [Online]. Available: http://dare.uva.nl/search?identifier=a2cc6d71-a434-458a-a06b-e8604978a117

[12] E. C. Fear, S. C. Hagness, P. M. Meaney, M. Okoniewski, and M. A. Stuchly, "Enhancing breast tumor detection with near-field imaging," *IEEE Microwave Magazine*, vol. 3, no. 1, pp. 48–56, Mar. 2002.

[13] T. Voigt, O. Väterlein, C. Stehning, U. Katscher, and J. Fiehler, "In vivo glioma characterization using mr conductivity imaging," 2010.

[14] X. Zhang, P.-F. Van de Moortele, S. Schmitter, and B. He, "Complex B1 Mapping and Electrical Properties Imaging of the Human Brain using a 16-channel Transceiver Coil at 7t," *Magnetic resonance in medicine : official journal of the Society of Magnetic Resonance in Medicine / Society of Magnetic Resonance in Medicine*, vol. 69, no. 5, pp. 1285–1296, May 2013. [Online]. Available: http://www.ncbi.nlm.nih.gov/pmc/articles/PMC3549472/

[15] T. Voigt, U. Katscher, and O. Doessel, "Quantitative conductivity and permittivity imaging of the human brain using electric properties tomography," *Magnetic Resonance in Medicine*, vol. 66, no. 2, pp. 456–466, Aug. 2011. [Online]. Available: http://onlinelibrary.wiley.com/doi/10.1002/mrm.22832/abstract

[16] J. Liu, X. Zhang, P.-F. Van de Moortele, S. Schmitter, and B. He, "Determining Electrical Properties Based on B1 Fields Measured in an MR Scanner Using a Multi-channel Transmit/Receive Coil: a General Approach," *Physics in medicine and biology*, vol. 58, no. 13, pp. 4395–4408, Jul. 2013. [Online]. Available: http://www.ncbi.nlm.nih.gov/pmc/articles/PMC3770135/

[17] X. Zhang, J. Liu, and B. He, "Magnetic Resonance Based Electrical Properties Tomography: A Review," *IEEE reviews in biomedical engineering*, vol. 7, pp. 87–96, 2014. [Online]. Available: http://www.ncbi.nlm.nih.gov/pmc/articles/PMC4113345/

[18] J. Liu, P. F. V. d. Moortele, X. Zhang, Y. Wang, and B. He, "Simultaneous Quantitative Imaging of Electrical Properties and Proton Density From $_1$ Maps Using MRI," *IEEE Transactions on Medical Imaging*, vol. 35, no. 9, pp. 2064–2073, Sep. 2016.

[19] R. L. Sacco, S. E. Kasner, J. P. Broderick, L. R. Caplan, J. J. B. Connors, A. Culebras, M. S. V. Elkind, M. G. George, A. D. Hamdan, R. T. Higashida, B. L. Hoh, L. S. Janis, C. S. Kase, D. O. Kleindorfer, J.-M. Lee, M. E. Moseley, E. D. Peterson, T. N. Turan, A. L. Valderrama, and H. V. Vinters, "An Updated Definition of Stroke for the 21st Century: A Statement for Healthcare Professionals From the American Heart Association/American Stroke Association," *Stroke*, vol. 44, no. 7, pp. 2064–2089, Jul. 2013. [Online]. Available: http://stroke.ahajournals.org/content/44/7/2064

[20] K. A. Hossmann and W.-D. Heiss, *Textbook of Stroke Medicine*, 2nd ed. Cambridge University Press, New York, USA, 2014.

[21] D. A. Warrell, T. M. Cox, J. D. Firth, and M. B. Edward J., J R., *Oxford Textbook of Medicine*, 4th ed. Oxford, UK: Oxford University Press, 2003. [Online]. Available: //oxfordmedicine.com/10.1093/med/9780199204854.001.1/med-9780199204854

[22] A. van Lier, A. Kolk, M. Brundel, J. Hendriske, J. Luijten, P. Lagendijk, and C. van den Berg, "Electrical conductivity in ischemic stroke at 7.0 tesla: A case study," vol. 20, ISMRM (International Society Magnetic Resonance in Medicine). 20th Annual Meeting of ISMRM, 2012, p. 3484.

[23] S. Semenov, T. Huynh, T. Williams, B. Nicholson, and A. Vasilenko, "Dielectric properties of brain tissue at 1 GHz in acute ischemic stroke: Experimental study on swine," *Bioelectromagnetics*, vol. 38, no. 2, pp. 158–163, Feb. 2017. [Online]. Available: http://onlinelibrary.wiley.com/doi/10.1002/bem.22024/abstract

[24] S. Y. Semenov, R. H. Svenson, and G. P. Tatsis, "Microwave Spectroscopy of Myocardial Ischemia and Infarction. 1. Experimental Study," *Annals of Biomedical Engineering*, vol. 28, no. 1, pp. 48–54, Jan. 2000. [Online]. Available: https://link.springer.com/article/10.1114/1.253

[25] M. N. Sadiku, *Theory of Electromagnetics*, 3rd ed. New York, N.Y., USA: Oxford University Press, 2002.

[26] S.-K. Lee and S. B. B. Bulumulla, "Efficient tissue permittivity and conductivity mapping using standard mr images," vol. 21, ISMRM (International Society Magnetic Resonance in Medicine). Salt Lake City: 21st Annual Meeting ISMRM, 2013, p. 3372.

[27] S. K. Lee, S. Bulumulla, F. Wiesinger, L. Sacolick, W. Sun, and I. Hancu, "Tissue Electrical Property Mapping From Zero Echo-Time Magnetic Resonance Imaging," *IEEE Transactions on Medical Imaging*, vol. 34, no. 2, pp. 541–550, Feb. 2015.

[28] S. K. Lee, S. Bulumulla, P. Lamb, and I. Hancu, "Measurement of electrical properties of biological tissue at radio frequencies using magnetic resonance imaging," in *2015 9th European Conference on Antennas and Propagation (EuCAP)*, May 2015, pp. 1–4.

[29] E. M. Haacke and J. A. Tkach, "Fast MR imaging: techniques and clinical applications." *American Journal of Roentgenology*, vol. 155, no. 5, pp. 951–964, Nov. 1990. [Online]. Available: http://www.ajronline.org/doi/abs/10.2214/ajr.155.5.2120964

[30] D. Ireland, K. Bialkowski, and A. Abbosh, "Microwave imaging for brain stroke detection using Born iterative method," *Antennas Propagation IET Microwaves*, vol. 7, no. 11, pp. 909–915, Aug. 2013.

[31] I. Bisio, A. Fedeli, F. Lavagetto, G. Luzzati, M. Pastorino, A. Randazzo, and E. Tavanti, "Brain stroke detection by microwave imaging systems: Preliminary two-dimensional numerical simulations," in *2016 IEEE International Conference on Imaging Systems and Techniques (IST)*, Oct. 2016, pp. 330–334.

[32] Y. Wu, M. Zhu, D. Li, Y. Zhang, and Y. Wang, "Brain stroke localization by using microwave-based signal classification," in *2016 International Conference on Electromagnetics in Advanced Applications (ICEAA)*, Sep. 2016, pp. 828–831.

[33] A. Zamani, A. T. Mobashsher, B. J. Mohammed, and A. M. Abbosh, "Microwave imaging using frequency domain method for brain stroke detection," in *2014 IEEE MTT-S International Microwave Workshop Series on RF and Wireless Technologies for Biomedical and Healthcare Applications (IMWS-Bio2014)*, Dec. 2014, pp. 1–3.

[34] (2010) The foundation for research on information technologies in society (IT'IS). [Online]. Available: https://www.itis.ethz.ch/virtual-population/tissue-properties/database/dielectric-properties

[35] DICOM homepage. National Electrical Manufacturers Association (NEMA). [Online]. Available: http://dicom.nema.org

[36] DICOM ps3.6 2016e - data dictionary, 6.registry of DICOM data elements. DICOM standards committee. [Online]. Available: http://dicom.nema.org/medical/dicom/current/output/html/part06.html

[37] DICOMlookup. [Online]. Available: http://dicomlookup.com

[38] Z. Wu, S. Mittal, K. Kish, Y. Yu, J. Hu, and E. M. Haacke, "Identification of calcification with MRI using susceptibility-weighted imaging: a case study," *Journal of magnetic resonance imaging: JMRI*, vol. 29, no. 1, pp. 177–182, Jan. 2009.

[39] C. B. Ahn and Z. H. Cho, "A New Phase Correction Method in NMR Imaging Based on Autocorrelation and Histogram Analysis," *IEEE Transactions on Medical Imaging*, vol. 6, no. 1, pp. 32–36, Mar. 1987.

[40] MathWorks, understanding waveletes. [Online]. Available: https://www.mathworks.com/videos/series/understanding-wavelets-121287.html

[41] U. Katscher, K. Djamshidi, T. Voigt, M. Ivancevic, H. Abe, G. Newstead, and J. Keupp, "Estimation of Breast Tumor Conductivity Using Parabolic Phase Fitting," in *Adapting MR in a Changing World: ISMRM 20th Annual Meeting, Melbourne*, vol. 20. ISMRM (International Society Magnetic Resonance in Medicine), Jun. 2012, p. 3482. [Online]. Available: http://dev.ismrm.org/2012/3482.html

Appendix A - attachment description

CD content:

- Master thesis .pdf
- MATLAB codes for simulations
- MATLAB code for MREPT
- Scan of the master's thesis assignment
- Keywords
- Abstract
- Abstract in Czech

Appendix B - statistical data from simulations and MREPT results

Table 11: *Statistical data used to estimate size of region of interest (ROI) for virtual samples (simulations). HS: hemorrhagic stroke, WM: white matter, IS: ischemic stroke. Values out of the range 1<x<100 for ε_r, and 0<x<4 for σ, were deemed corrupted.*

	$\varepsilon_r(-)$			$\sigma(\mathrm{S}\cdot\mathrm{m}^{-1})$		
	HS	WM	IS	HS	WM	IS
Mean	76,5	52,3	46,6	1,21	0,33	0,17
Variance	44,69	28,47	48,90	0,0094	0,0012	0,0016
Std. Deviation	6,68	5,34	6,99	0,0971	0,0349	0,0405
Computed data points	1637	1625	1955	1680	1690	1897
Total data points	1637	1711	1955	1681	1690	1919
Percentage computed data	100%	95%	100%	100%	100%	99%
Percentage corrupted data	0%	5%	0	0%	0%	1%
ROI size	687	438	751	40	5	7
Applied ROI size	693	420	780	49	6	9

Table 12: *Statistical data used to estimate size of region of interest (ROI) for real samples within simplified head phantom (MREPT). HS: hemorrhagic stroke, WM: white matter, IS: ischemic stroke. Values out of the ranges 1<x<100 for ε_r, and 0<x<4 for σ, were deemed corrupted.*

	$\varepsilon_r(-)$			$\sigma(\mathrm{S}\cdot\mathrm{m}^{-1})$		
	HS	WM	IS	HS	WM	IS
Mean	80,7	59,0	49,5	1,21	0,38	0,15
Variance	81,15	19,96	27,85	0,006	0,100	0,057
Std. Deviation	9,0	4,5	5,3	0,08	0,32	0,24
Computed data points	587	665	674	730	714	657
Total data points	914	926	921	1443	1443	974
Percentage computed data	64%	72%	73%	51%	49%	67%
Percentage corrupted data	36%	28%	27%	49%	51%	33%
Sample size	312	307	428	25	426	241
error (e)	1	0,5	0,5	0,03	0,03	0,03
Applied sample size	324	324	441	25	441	256

Appendix C - phase histogram distributions of SE images correction

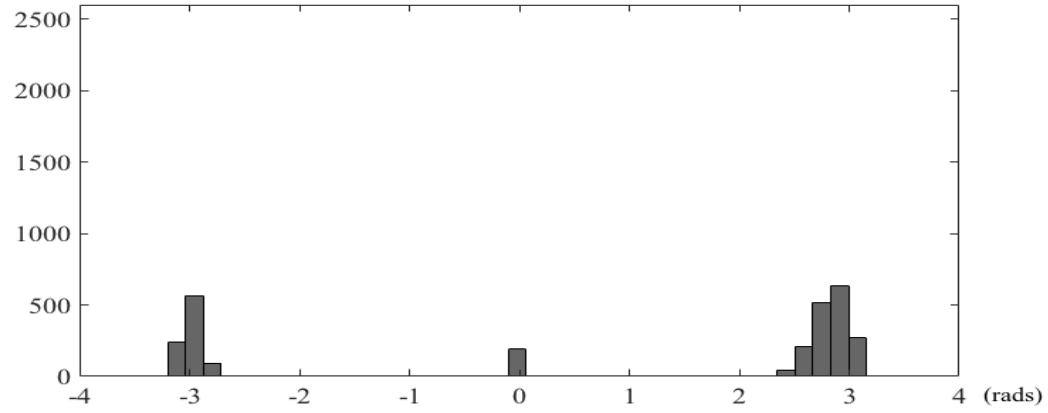

(a)

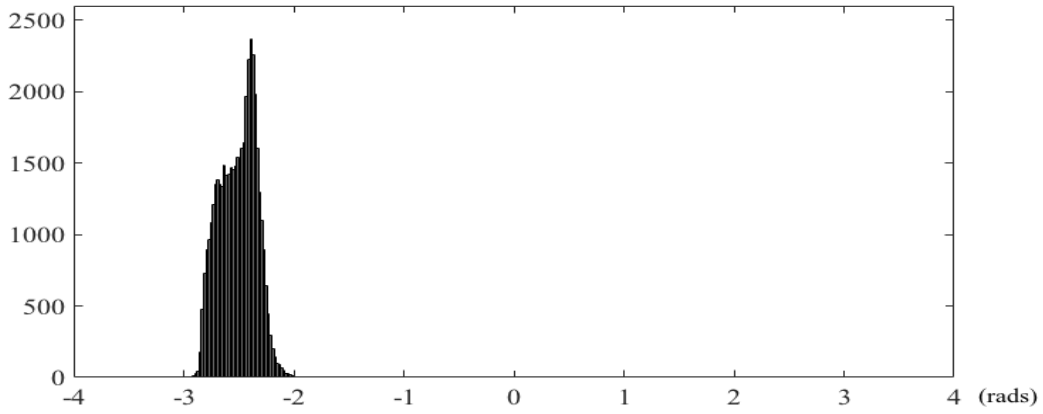

(b)

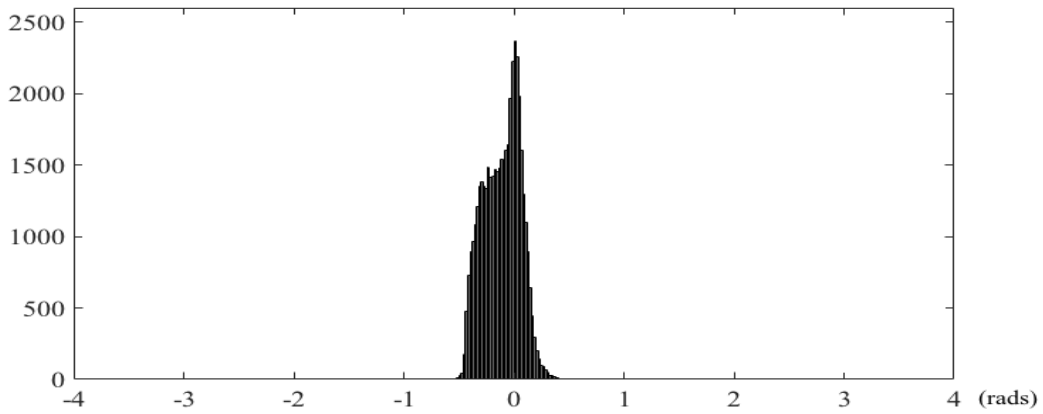

(c)

Figure 23: *Histograms SE phase correction a) Original SE phase histogram. b) SE Phase histogram after first-order (ϵ_1) phase correction. c) SE Phase histogram (final) after zero-order (ϕ_0) phase correction*